Dynamic Benthic Oxygen Fluxes Lessen Hypoxia Effects on Open Continental Shelves

Clare E. Reimers[1*], Sarah K. Henkel[2], Kristen E. Fogaren[1,3], Peter J. Chace[1], Anna Hughes[1] and W. Waldo Wakefield[4]

[1]College of Earth, Ocean, and Atmospheric Sciences, Oregon State University, Corvallis, Oregon, 97331, USA

[2]Department of Integrative Biology, Oregon State University, Corvallis, Oregon, 97331, USA

[3] Current address: Earth and Environmental Sciences, Boston College, Chestnut Hill, MA 02467, USA

[4]Cooperative Institute for Marine Ecosystem and Resources Studies (CIMERS), Oregon State University, 2030 SE Marine Science Drive, Newport, Oregon 97365, USA

*Correspondence: clare.reimers@oregonstate.edu

Other Author Email addresses: sarah.henkel@oregonstate.edu, fogaren@bc.edu, chacep@oregonstate.edu, hugheann@oregonstate.edu, waldo.wakefield@oregonstate.edu.

Running Head: Oxygen fluxes to a shelf benthos under hypoxia

Abstract

Under the supposition that organisms inhabiting physically dynamic marine environments are better able to survive hypoxic conditions than those experiencing little turbulent or advective augmentation of oxygen fluxes, we evaluated summertime benthic macrofauna communities, in situ aquatic eddy covariance measurements, and ex situ sediment core incubations from 5 latitudinally distinct mid-shelf locations off Oregon-Washington, USA. Despite bottom water dissolved oxygen (DO) concentrations averaging from 17-75 μmol L^{-1}, invertebrate faunal collections contained mixtures of 11-28 taxa per 0.1 m^2 box core and increased in richness and abundance at sites with greater velocity variation. Eddy covariance derivations showed that oxygen fluxes to the shelf benthos are very often correlated with flow parameters and with short-term changes in DO that are associated with internal waves. Daily averages of the oxygen fluxes to the sediment were determined to range from -3.5 to -23 mmol $m^{-2}d^{-1}$, and these fluxes, assumed to fully represent seabed respiration, were 2-5 times greater than rates of DO uptake by sediment cores from the same locations. Velocity profiles measured from 0.3 to 2.5 m above the seafloor at a subset of sites were consistent with a wave-current boundary layer modulated by ocean swell. These findings illustrate how natural physical processes can relieve the stress of hypoxia exposure on the benthos. Physical dynamics play critical roles in supplying DO and determining sediment grain size, permeability, and the activities of benthic organisms. Thus, these factors need consideration when predicting the impacts of low DO concentrations in coastal regions.

Introduction

The prevalence and severity of oxygen depletion in coastal waters are increasing worldwide with consequences affecting marine life, biogeochemical processes, and ecosystems (Diaz and Rosenberg 2008; Rabalais et al. 2010; Breitburg et al. 2018). Low oxygen waters are causative of what have been characterized as "dead zones" and are described as "hypoxic" when dissolved oxygen (DO) concentrations are ≤2 mg L^{-1} (62.5 μmol L^{-1}) (Rabalais et al. 2002). However, previous studies demonstrate wide ranges of thresholds for lethal and sublethal responses to low oxygen among different marine taxa (Vaquer-Sunyer and Duarte 2008). Sublethal responses include avoidance as well as significant changes in respiration, ventilation, feeding, growth, and reproductive rates (Lee et al. 2023). Additionally, an organism's normal mobility, life stage, and habitat associations affect these responses, with, for example, many sessile organisms relying on pumping behaviors or stirring actions to augment molecular diffusion for oxygenating tissues (Hoffman et al. 2008; Shapiro et al. 2014). Different thresholds can also be explained as reflecting a diversity of physiological and biochemical systems evolved within organisms as defense mechanisms to hypoxia (Levin et al. 2009; Somero et al. 2016; Lee et al. 2023). The most effective mechanisms clear anaerobic metabolites that cause oxidative stress and are believed to be linked to the expression of specialized hypoxia induction factor genes in many hypoxia-tolerant invertebrates (Lee et al. 2023).

Whether caused by natural or anthropogenic factors, hypoxic waters will form in coastal locations with high rates of sub-pycnocline, water-column respiration and benthic respiration fueled by organic matter fluxes (Fennel and Testa 2019). In many regions, these conditions are seasonal, and in some instances, hypoxic waters may extend from their source regions due to coastal upwelling and other drivers of physical advection governed by wind, bathymetry,

63 circulation, and stratification (Adams et al. 2016; Jarvis et al. 2021; Walter et al. 2022). Physical
64 dynamics will also drive oxygen variability over a range of frequencies in marine environments,
65 making it challenging to link specific oxygen levels to observations of mortalities of organisms
66 in the field or to changes in benthic communities (Rabalais et al. 2002; Vaquer-Sunyer and
67 Duarte 2008). Further, depending on the physiological mechanisms and anatomical adaptations
68 an organism uses to take up dissolved oxygen (DO), the physical processes that govern the flux
69 of gases to a boundary may outweigh the environmental oxygen concentration in dictating the
70 organism's oxygen uptake rate and susceptibility to hypoxia. Take, for example, the many
71 benthic marine mollusks, cnidarians, echinoderms, and annelids that exchange gases through
72 protruding tube feet, tenacles, ciliated gills, or their epidermis (Storch and Alberti 1978; Perry et
73 al. 2019). These body surfaces are living boundaries within the environment's benthic boundary
74 layer (BBL), which encompasses both waters in direct contact with the seafloor and the
75 uppermost layers of seafloor substrates (Boudreau and Jørgenson 2001). At positions
76 approaching organism and sediment interfaces, the supply of DO will depend on highly variable
77 contributions from advection, turbulent eddies, and molecular diffusion (Boudreau 1997). The
78 supply will be influenced by flow patterns over or through an organism's body (Abelson et al.
79 1993), roughness elements of the habitat, and the permeability of the substrata where microbial
80 respiration usually dominates (Glud 2008). Advection and turbulence may also cause sediment
81 resuspension and transport, altering sediment texture and bedforms. On open (specifically,
82 pericontinental) shelves, currents, deep-reaching wave action, and high turbulence appear to
83 enable many metazoan species to persist and be active under low DO conditions while also
84 enhancing oxygen consumption and limiting organic matter burial. These factors have the

85 potential to set open shelves apart from many continental slopes, semi-enclosed basins, fjords,
86 and bays when characterizing benthic communities under hypoxia (Levin et al. 2009).
87 The focus of this paper is to use observations from the Oregon-Washington continental
88 shelf to illustrate the highly dynamic nature of the supply of DO to benthic communities on an
89 open shelf during periods of oxygen depletion. We present a combination of invertebrate
90 community characterizations, in situ eddy covariance measurements, and ex situ sediment core
91 incubations from five mid-shelf areas sampled between 44.5 and 46.5°N during short-duration,
92 summer, oceanographic research cruises in 2018 or 2022. Near-bed velocity profiles are added
93 from three areas. We make the reasonable but rarely considered argument that organisms
94 inhabiting physically dynamic marine environments like the Oregon-Washington shelf are better
95 able to survive hypoxic conditions than those experiencing little DO exchange coupled to
96 advection and turbulent mixing. Further, we explore the dynamic and environmental variables
97 that may explain variation in benthic oxygen fluxes as determined by the eddy covariance
98 method that has been validated in many prior studies and found to be non-invasive and able to
99 detect the effects of faunal activities and flow on benthic oxygen uptake (Berg et al. 2003, 2022).

100 ***Materials and methods***

101 **Seabed characteristics, communities, and sample collections**

102 Oregon-Washington shelf sediments at water depths less than 100 m are dominantly
103 composed of fine sand (both relict and modern; Goldfinger et al. 2014), are subject to active
104 erosion, transport, and rippling by waves and currents in winter, but collect fresh phytodetritus
105 and finer surface deposits in summer (Komar et al. 1972; Kulm et al. 1975; McCann-Grosvenor
106 et al. 2014). At mid-shelf depths, the surface sediments become highly bioturbated in the
107 summer, losing ripple marks but gaining mounds, depressions, tracks, and burrows (Kulm et al.

1975). Demersal fishes and large benthic invertebrates, including the commercially important Dungeness crab (*Metacarcinus magister*), are moderately abundant and have catch rates per unit effort in fisheries bottom trawl surveys that are positively related to bottom water DO (Keller et al. 2010, 2015). Assemblages of smaller invertebrate macrofauna that serve as prey for many flatfishes (Kravitz et al. 1977; Pearcy and Hancock 1978) are patchy and group largely by sediment grain size and water depth (Henkel and Gilbane 2020), with latitudinal gaps in species occurrence indicating other controlling factors (Henkel and Nelson 2018). The method to distinguish macrofauna applied by Henkel and Gilbane (2020) was to sample the seabed with a 0.1 m^2 Grey-O'Hara (aka GOMEX) box core (Boland and Rowe 1991) and to sieve the collected cores through a 1.0 mm mesh to assess the organisms living in the sediment or as epifauna. The same sample collection and processing methods were applied here and paired in 2022 with bottom images captured with two downward-looking Paralenz *Vaquitas* video cameras mounted with DeepSea Power & Light *SeaLites* on a wire-landed frame (74 cm x 74 cm). A towed video beam trawl system (Stinton et al. 2014) provided bottom imagery for a study location on the Newport Hydrographic (NH) Line sampled repeatedly in 2018, but since no box core collections were made at that site in 2018, we include macrofauna data from NH Line sampling in the summer of 2010. A hydraulically dampened gravity corer was used to recover cores for incubation studies and later core sectioning in both 2018 and 2022 (core tube inner area = 88.2 cm^2, methods described in Hughes et al. 2025). Fig. 1 displays the primary site locations on a regional bathymetric map with representative seabed images. The surface sediments are dominantly fine to medium sand with organic carbon contents universally less than 0.2% dry weight across all but the siltier area off Willapa, Washington (WLP1) (Reimers et al. 2012; Hughes et al. 2025). At WLP1, the median grain size was determined to be 43 μm, and the

organic carbon was 1%, reflecting inputs from the Columbia River (Hughes et al. 2025). Sediment permeability has been measured using core samples from the NH80 site (Reimers et al. 2012) and at the PWS2 site (Reimers, unpublished), equating to 1.7-3.9 x 10^{-11} m^2, which is a typical range for medium sand (Huettel and Rusch 2000).

Oceanographic setting

Hypoxia develops on the Oregon-Washington continental shelf only during the summer upwelling season, and its prevalence has increased over the past half century (Chan et al. 2008; Pierce et al. 2012; Barth et al. 2024). When viewed from the perspective of the region's physical drivers, hypoxia occurs primarily because oxygen-depleted waters from offshore are advected onto the shelf by intermittent, wind-driven Ekman transport and then retained as bottom waters in areas of enhanced stratification or sluggish BBL flow (Adams et al. 2016). BBL heights on the shelf, when defined by isopycnals, DO, and turbidity, are generally 10-30 m; however, they have event-scale variability dictated by upwelling strength (Perlin et al. 2005; Adams et al. 2016). Generally, the BBL will thicken during wind relaxations or downwelling. At certain locations, BBL thickness and DO are also affected by local recirculation and sources of turbulence, such as when flow meets a topographic high or when internal waves propagate onto the shelf (Moum et al. 2007; Siedlecki et al. 2015).

The second contributor to hypoxia on the Oregon-Washington shelf is local DO consumption. Water-column respiration combined with sediment oxygen demand is estimated to generate at least 50% of the oxygen deficit and to oxidize roughly 60-70% of the organic matter produced during a typical upwelling season (Connelly et al. 2010; Siedlecki et al. 2015). Thus, the DO and density signature of water upwelled onto the shelf is progressively altered by biological processes and by shelf mixing (Pierce et al. 2012). Fig. 2 displays illustrative lower

water column DO and density profiles collected over each study location by casts of Sea-Bird CTD packages with SBE-43 oxygen sensors. The NKW1 site, named for its location off Neskowin, Oregon (see also Hughes et al. 2025), is the shallowest of this study's primary sites, is located where the shelf is narrowest, and was oxygen-depleted but not hypoxic when sampled. For characterizing the 80 m site on the Newport Hydrographic Line (also designated by some researchers as NH10 because it is 10 nm from shore), there is the added benefit of long-term, ship-based, mooring, bottom-node, and glider water-column data and time-lapse imagery stemming from the Ocean Observatories Initiative and earlier programs (Risien et al. 2023). For example, OOI data products during the summer of 2018 show that the bottom waters at NH80 were hypoxic nearly continuously during August, with a similar prolonged period of low DO in August 2022 (https://ooinet.oceanobservatories.org).

Eddy covariance measurements

The principal outcomes of this study will be drawn from seven eddy covariance lander deployments, with these deployments numbered in order of deployment dates. Deployments 1-3 were at the NH80 site and will be used to compare fluxes replicated across a site and within a single summer season: 2018. Deployments 4-7 occurred in 2022 at PWS2, NKW1, NEH2, and WLP1, respectively.

The primary eddy covariance measurements were water-column velocities and DO concentrations. Velocities were measured in Cartesian *xyz* coordinates (referenced to the instrument) using a fixed-stem Nortek *Vector* Acoustic Doppler Velocimeter (ADV). The ADV was oriented vertically with its probe directed down and clamped at a position that nominally placed the acoustic sampling volume 30 cm above the seafloor (see *Supporting Information* Fig. S1a). However, the true height above the seafloor was also measured by the *Vector* from a

bottom echo at the start of each deployment and ranged from 27-31 cm. Additionally, the ADV recorded pressure, as well as compass heading, pitch, and roll, which allowed transformation of *xyz* velocities into East-North-Up (ENU) coordinates where a positive E velocity is towards East. DO was measured with 430 μm-diameter Pyroscience fiber-optic oxygen sensors (OXB430) positioned with tips ~2 cm outside the ADV's sampling volume. In one case, we report results obtained when a pair of OXB430 sensors was used with a single ADV, and each fiber was oriented at a position opposite a different receiver probe of the *Vector,* such that the tips were separated by 120° in the plane of the ADV sampling point (Fig. S1b).

Two nearly identical aluminum lander frames, moored to floats at the sea surface, were the deployment and recovery platforms for the eddy covariance sensors as described previously (Reimers et al. 2012, 2016; Reimers and Fogaren 2021). Reference measurements included records from co-located Aanderaa oxygen optode/temperature (model 4175) sensors or a Sea-Bird 16plusV2 CTD. Additionally, near-bottom temperature, salinity, and DO reference measurements were made at 2-5 discrete times during lander deployment periods through casts of the ship's Sea-Bird CTD sensor package.

Derivations of eddy covariance oxygen fluxes and parameters

To derive eddy covariance oxygen fluxes, a data processing sequence described in detail within the *Supporting Information* was followed. Briefly, the time series of measurements from each deployment were divided into 15-minute-long data segments or "bursts"; trends in the directional velocities and oxygen concentrations were computed as 6.25-min running averages (but also compared to other mean estimates); and the varying components $[v_x'(t), v_y'(t), v_z'(t), C'(t)]$ were derived by subtraction of trend points from measurements at

corresponding times. After these and other steps to finalize the time series of v_z' and C', estimates of total eddy covariance oxygen flux by burst were calculated as

$$Oxygen\ flux = \overline{v_z'C'} \quad (1)$$

where the overbar $\overline{\ }$ denotes a time average (Berg et al. 2003, 2022).

Additionally, burst averages of all measured parameters and a variety of other derived parameters were computed routinely. Amongst the derived parameters, several represented characteristics of the physical environment, including horizontal flow speeds (*S*) computed as

$$S = \sqrt{\overline{v_x}^2 + \overline{v_y}^2} \quad (2)$$

(Trowbridge and Lentz 1998) where any uncertainty created by signal noise was minimized by first averaging the velocity components of each burst. Similarly, friction velocities (u_*) were calculated based on Reynolds stresses, according to the covariance technique relationship as

$$u_* = ((\overline{v_x'\ v_z'})^2 + (\overline{v_y'\ v_z'})^2)^{1/4} \quad (3)$$

(Berg et al. 2007); and pressure-based, bottom-sensed significant wave heights (H_s); root-mean-square (RMS) wave-induced velocities; and turbulent dissipation rates (ε) were calculated as in Reimers et al. (2012), Trowbridge and Agrawal (1995), and Reimers et al. (2020), respectively.

Further, we considered that flux variations may stem from factors affecting one or both the covariate measures, i.e., v_z' or C', and we characterized the strength of these variations as $sv_z' = (\overline{|v_z'|})$ and $sC' = (\overline{|C'|})$. Conceptually, situations could arise where benthic oxygen uptake rates increase under unchanging flow (for example, due to fresh organic matter inputs), resulting in a flux correlation with sC' but not with sv_z'. Conversely, heightened turbulence reflected in sv_z' may drive more DO into permeable shelf sediments, enhancing oxygen uptake rates because of greater oxidation of reduced pore water solutes.

Correlations between these parameter averages and oxygen fluxes within and between deployments were assessed by computing pairwise Pearson's correlation coefficients (r) and p-values (setting significance for $p<0.05$) using OriginPro 2024 data analysis and graphing software after expressing the fluxes as positive sediment oxygen consumption rates. We also applied a circular-linear correlation analysis between flow direction and flux using a Matlab toolbox developed by Berens (2009).

BBL velocity profiles

To further characterize BBL dynamics during hypoxia, vertical velocity profiles were measured spanning 0.3 to 2.5 m above the seafloor using a Nortek Aquadopp HR, 1 MHz, side-looking acoustic profiler fixed horizontally in an upward-facing configuration and set on the seafloor as an extension off a wire-lowered tripod (1.6 m pod-to-pod, 1.4 m high) (see *Supporting Information* Fig. S2). The Aquadopp was deployed only during the 2022 cruises, and it sampled at 1 Hz. Profiles were selected from casts where the instrumentation was stable on the seafloor for >2-5 min. The lowest sampling height of these measurements was determined by the setting of the Aquadopp's acoustic blanking distance and its face height above the seafloor. The period and height of surface waves sensed near the bottom were derived from the Aquadopp's time series of pressure with the same code applied to *Vector* time series of pressure (Reimers and Fogaren 2021). Lastly, logarithmic regressions of lower segments of mean flow speed profiles were computed to assess how well profiles conformed to the standard law of the wall model for turbulent flow and to yield additional estimates of friction velocities (u_*) and large-scale roughness parameters (z_o) at each site (Trowbridge and Lentz 1998, 2018). The model was applied assuming that the average near-bottom horizontal flow speed (S) will vary with height above the seafloor (z) according to the relationship

$$S = \sqrt{\bar{E}^2 + \bar{N}^2} = \frac{u_*}{\mathrm{K}} \ln\left(\frac{z}{z_o}\right) \quad (4)$$

where $\bar{E}$ and $\bar{N}$ are means of the measured velocities in East and North coordinates, and K is the von Karman's constant (0.41). Only the lowest five profile bins were fit to the model in keeping with previous studies that have suggested that more than one logarithmic-profile region with different logarithmic slopes may develop (Chriss and Caldwell 1982). Profile-based friction velocities were also compared to concurrent covariance technique derivations (Eq. 3) in three cases.

Macrofaunal taxonomic analysis

Upon return to the laboratory, organisms sieved from box core samples collected from a small range of water depths proximate to the eddy covariance lander deployment locations were sorted into major taxonomic groups. Echinoderms were identified by laboratory staff, and crustaceans, mollusks, and polychaetes were sent to contracted taxonomic experts. Multivariate analyses were undertaken using PRIMER 7th Edition (Clarke and Gorley 2006). Species abundance data were square-root transformed to reduce the influence of highly abundant species. A Bray-Curtis similarity matrix was created as the basis for investigating variability in communities among stations. The SIMPER routine in PRIMER was run to identify the characteristic species (taxa that are primarily responsible for observed differences between groups of samples) of each site and their densities. Biological traits of characteristic fauna were obtained from Queirós et al. (2013) and the Cefas Data Portal (https://data.cefas.co.uk/#/View/21362) developed by Clare et al. (2022).

Results

Benthic macrofaunal assemblages

Fig. 2 established that severe to borderline hypoxic conditions were present in the bottom waters above the shelf sediments sampled in this study. However, from these sediments, macrofauna invertebrates were collected in densities averaging 31-113 organisms per 0.1 m^2 box core per sampling area, and these samples contained on average 11 to 28 taxa (Table 1). Characteristic taxa differed among locations with some latitudinal patterns. Although faunal abundance and richness estimates near the NH80 site were derived from box core sampling in the summer of 2010, helically coiled gastropods (appearing to be *Alia gausapata*) were abundant on the seafloor in bottom video imagery collected in 2018 (Fig. 1), as well as in 2010 (Table 1). Megafauna visible in the 2018 bottom imagery included fishes (Pacific sanddabs *Citharichthys sordidus*, English sole *Parophrys vetulus*, Dover sole *Microstomus pacificus*, Rex sole *Glyptocephalus zachirus*, Longnose skate *Caliraja rhina)*, anemones, and sea stars. Fresh mounds, burrow openings, tracks, tubes, and decaying detrital pyrosomes (cf. *Pyrosoma atlanticum*) were common (see *Supporting Information* Fig. S3).

One organism of special interest is the burrowing shrimp, *Neotrypaea gigas*, which is known to inhabit both shelf and estuarine sediments, but was first noted in high densities on the Oregon shelf just inshore of the PWS2 site in 2019 (Henkel et al. 2022). This discovery caused us to hypothesize that *Neotrypaea gigas* may be shifting its distribution and/or abundance and thus affecting other resident macrofauna because of its deep burrow digging and irrigation. Burrow openings presumed to be from *Neotrypaea gigas* (but also documented in gravity cores) were visible in drop camera videos at all four sites sampled in 2022 (Table 1), and shrimp were recovered in densities up to 15 per box core or 150 m^{-2}. Flow from burrow openings was observed in drop camera videos, indicating active burrow maintenance.

Eddy covariance time series

289 The BBL dynamics of the Oregon-Washington shelf in summer were sampled by this
290 study's eddy covariance measurements, with Fig. 3 illustrating deployments 1 and 3 from the
291 Newport Hydrographic Line site at 80 m (NH80). Common features of the near-bed velocity
292 series (top panels) are the combined effects of surface wave oscillations and currents, internal
293 wave arrivals, and tides. Oxygen concentrations (middle panels) show periods of both stability
294 and change, often with gradual increases or declines following shifts in the tide. Pressure time
295 series (middle panels) indicate the timing of tides, and the period and the height of the surface
296 swell. The 15-min flux determinations displayed in the bottom panels are the basis for flux
297 averages (± 1 standard deviation) given in Table 2 with other situational information for all
298 deployments. A summary of all derived flow parameters, such as mean horizontal flow speeds
299 and friction velocities, is given by deployment in *Supporting Information* as Table S1.
300 Close examinations of the combined sensor records from individual deployments reveal
301 further details of the regional summertime hydrodynamics. First, internal waves crossing a site
302 may impact velocities greatly while having little effect on oxygen concentrations as was
303 observed between ~17:00 and 19:00 on July 3, 2018, at NH80 (Fig. 3a) and more strikingly
304 between ~01:30 and 3:00 on August 3 (Fig. 3b). Second, small temperature changes may roughly
305 mirror small oxygen changes over cycles of mixed tides (for example, declines of <0.02°C when
306 DO declined 2-3 μmol L^{-1} toward the low tides at the NH80 site in August, see Fig. S8 in
307 *Supporting Information*). Further, horizontal flow speeds can be relatively low, averaging 5.0 ±
308 2.4 cm s^{-1} during deployment 1 and only 3.3 ± 1.7 cm s^{-1} during deployment 3 under quiescent
309 BBL conditions influenced primarily by the summertime swell. The two co-occurring
310 independent deployments of separate eddy covariance systems landed 0.4 km apart at NH80 in
311 July 2018 (deployments 1 and 2) represent a full duplication of the approach under shared

312 bottom water conditions. The two deployments yielded nearly equivalent average fluxes (Table
313 2) and velocity records that confirmed shared regional forcings but also differences in local
314 friction velocities (Fig. 4).

315 The July 2022 record from the southern-most site PWS2 (see *Supporting Information*
316 Fig. S5) had average flow speeds of 4.6 ± 2.5 cm s^{-1}, which were observed during more acutely
317 hypoxic conditions (average DO = 24.7 ± 1.2 μmol L^{-1}, Table 2) than observed at NH80 in 2018.
318 During the PWS2 deployment, internal wave arrivals were also seen in the velocities, and these
319 waves were accompanied by oscillations and small rises in the dissolved oxygen concentration.
320 Oxygen fluxes at the PWS2 site averaged -4.9 ± 2.3 mmol m^{-2} d^{-1}.

321 During the NEH2 deployment (Fig. 5), two fiber optic oxygen sensors measured oxygen
322 variations separately on one lander to yield two oxygen flux records that helped to identify an
323 example of an intermittent sensor artifact (Huettel et al. 2020). Sensor "ox1" displayed some
324 sharp jumps in signal near the end of the deployment that were not recorded by "ox2". This
325 sensor instability led to lower ox1 fluxes over the last 5 bursts, even when these data segments
326 were trimmed to remove the most egregious spikes. However, the temporal variations in fluxes
327 seen over the whole preceding record are reflected by both sensors, increasing confidence that
328 the dynamics of the BBL extend to benthic oxygen fluxes. The overall bottom water oxygen
329 concentration also rose by 30 μmol L^{-1} over the 22.5-h NEH2 deployment, thereby approaching
330 the upper limit of hypoxia.

331 The average eddy covariance-derived oxygen flux at NEH2 in September 2022 was
332 -13.2 ± 6.9 mmol $m^{-2}d^{-1}$ (via ox 1, Table 2), but the site off Neskowin, Oregon, NKW1, during
333 the same week in September had notably higher oxygen concentrations and greater fluxes into
334 the sediment (-23.0 ± 11.2 mmol $m^{-2}d^{-1}$, Table 2). Oxygen concentrations observed 30 cm above

335 the seafloor of site NKW1 rose from 63 to 85 μmol L^{-1} with a very abrupt change coincident
336 with internal wave arrivals starting at ~21:00 in the record (see *Supporting Information* Fig. S6).
337 This site had benthic oxygen fluxes of magnitudes we have measured in past Oregon shelf
338 studies only at inner shelf depths in summer months (McCann-Grosvenor et al. 2014) or under
339 winter conditions on the mid shelf (Reimers and Fogaren 2021).
340 Lastly, WLP1 exhibited multiple episodes of internal wave arrivals and eddy covariance-
341 derived oxygen fluxes equaling -4.7 ± 2.6 while being under severely hypoxic conditions (see
342 *Supporting Information* Fig. S7). All eddy flux means were 2-5 times greater in magnitude than
343 corresponding core incubation fluxes (Table 2), indicating oxygen uptake enhancements are
344 created by turbulent flow across tens of m^2 of shelf sediment and bottom life (the eddy
345 covariance footprint, Berg et al. 2007).

346 **Exploration of covariate factors for eddy fluxes within records**

347 All the eddy covariance oxygen flux records of this study exhibited sub-hourly
348 variability. Pairwise Pearson correlation analyses were run to investigate which short-term
349 factors showed the greatest association (Fig. 6, *Supporting Information* Table S2). Interestingly,
350 the strength of the covariate measures, sv_z' and *sC',* both drove changes in the oxygen uptake,
351 with sv_z' dominating variations across deployment 5 (NKW1) compared to *sC'*; both measures
352 being of about equal importance within deployments 2, 4 and 7 (NH80#2, PWS2 and WLP1);
353 but *sC'* having a greater influence on flux variations during deployments 1, 3 and 6
354 (NH80#1and#3 and NEH2). Varying flow conditions recorded during deployments 1, 4, 5, 6 and
355 7 caused parameters such as u_* and ε to correlate significantly with short-term rates of sediment
356 oxygen uptake. Fluxes observed within deployments 1, 2, 6 and 7 were moderately correlated
357 with both RMS velocities and horizontal flow speed, but not with wave heights. In contrast,

fluxes during the August 2018 NH80 deployment 3 had weak correlations (r< |0.2|) with all flow-related parameters, reflecting the relatively quiescent conditions during that observation period.

Another question we sought to test was whether flux values depended on flow direction, which could occur if the seafloor was not uniform around the eddy covariance lander at a given site or if there were differential lander effects on the measurements. This led to circular-linear correlation computations between Dir (computed from E and N velocities) and flux. Only deployment 4 at the PWS2 site showed a moderately strong directional dependence (r= 0.44, p-value <0.0001, Table S2).

Exploration of covariate factors for eddy fluxes between deployments

When using correlation analyses between mean fluxes and environmental factors by deployment, many of the same variables examined within single records emerged as important, and pressure (station depth) was an added variable (see *Supporting Information* Table S3). Notably amongst the seven deployments, significant relationships between sediment oxygen consumption rates and mean determinations of sC', DO, and pressure were reflected in Pearson coefficients of 0.97, 0.68 and -0.78, respectively, indicating greater rates of oxygen uptake and thus larger oxygen fluctuations at shallower, more oxygenated sites. Pearson correlation coefficients found for relationships between sediment oxygen uptake rates and mean sv_z', Horizontal speed, RMS velocity, ε, and u_*were 0.73, 0.37, 0.77, 0.51 and 0.83, respectively, further supporting flux enhancements by physical dynamics. Bottom-sensed significant wave height H_s was only weakly correlated (r= 0.26), but wave height is expected to be largely a seasonal driver reflective of winter storm activity (Reimers et al. 2016). Median grain size, macrofaunal numbers, and richness were also tested for correlations with the mean oxygen

consumption rates of the four sites fully characterized in 2022, yielding non-significant correlation coefficients of 0.48, 0.51 and 0.45, respectively, and weaker correlations with mean DO. Macrofaunal abundance and richness did show significant correlations with mean sv'_z, turbulent dissipation rates, RMS velocities, and with each other, despite the low number of observations (see *Supporting Information* Table S4). The estimates of turbulent energy dissipation rates, ε, ranged on average from 3.7×10^{-7} to 7.8×10^{-6} m^2s^{-3} (see *Supporting Information* Table S2) in agreement with prior determinations by Perlin et al. (2005).

Velocity profiles

Additional observations for characterizing the BBL dynamics for three regions sampled in 2022 are presented through acoustic velocity profiles (Fig. 7) and log-layer fitting parameters (Table 3). The profiles capture only snapshots of the vertical structure of mean flow in the BBL, but they offer insight into the extent of deviations from the classical log-law, and apparent bottom roughness scales (z_o) affecting turbulent fluctuations and oxygen exchange near the bottom boundary. We note the tripod may have caused minor amounts of acoustic beam interference, especially with beam spreading above 1.2 m in some profiles. The time series of velocities and pressure measured with the Aquadopp profiler show that near-bottom flows were dominated by the local swell (see *Supporting Information* Fig. S9). Furthermore, the mean flow was directed primarily to the north within 2.5 m of the bottom during two NEH area casts and at WLP1 (Fig. 7). Flattening wave orbitals, bottom friction, and effects of the bottom Ekman layer balance (Perlin et al. 2005) appear to have created distinctive profile segments below approximately 0.6 m height. The cm-scale roughness lengths derived from the lowest profile segments at NKW1, WLP1, and NEH1 agree with observations from bottom images (Fig. 1), and the friction velocities fall within the ranges of values based on Reynolds stresses using the

404 covariance relationship (Table 3). In the case of the NKW1 profile, the measurements coincided
405 with an episode of internal wave arrivals evident in Fig. S6 of the *Supporting Information*. The
406 NEH2 profile, which was based on only a 2-minute record (Table 3), coincided with some of the
407 highest flow speeds observed late in the eddy covariance deployment at that site (Fig. 5).

408 ***Discussion***

409 In this study we focused on the middle Oregon-Washington shelf, a region where hypoxia
410 occurs because of physical and biogeochemical processes within a seasonal coastal upwelling
411 regime. We show that while the seafloor may be bathed by hypoxic waters, highly variable
412 physical dynamics within the benthic boundary layer will maintain a supply of oxygen to the
413 benthos, fueling consumption rates of -3.5 to -23 mmol m^{-2} d^{-1} during summer. The rates from
414 different sites varied inversely with water depth and directly with flow parameters such as
415 friction velocities. Greater confidence in these rates was established through concurrent
416 deployments of two eddy covariance landers in one experiment, by a repeat deployment at the
417 same site one month later, and by another deployment with dual DO sensors. The results from
418 these experiments suggest that rates of seabed respiration when averaged over 24 h are not
419 highly heterogeneous at shelf area scales of 0.2 km^2 or within a single summer season. They also
420 show that short-term variability within records is common and reproducible. Furthermore, these
421 eddy covariance benthic oxygen fluxes were significantly elevated over fluxes measured by
422 parallel core incubations (-1.2 to -4.3 mmol m^{-2} d^{-1}, Table 2). Prior diffusive oxygen utilization
423 rates from microelectrode oxygen profiles (-1.1 to -2.7 mmol m^{-2} d^{-1}, McCann-Grosvenor et al.
424 2014; Reimers et al. 2012) and prior in situ benthic chamber DO fluxes (-4.3 to -12.5 mmol $m^{-2}d^{-1}$
425 , Fuchsman et al. 2015) on the Oregon shelf in summer support the oft conclusion that core
426 incubations will underestimate rates of seafloor oxygen uptake simply because they do not

maintain the natural conditions of physical and biological advective exchange captured by eddy covariance (Jørgensen et al. 2022). However, oxygen fluxes can be dominated by diffusion in low-energy deep-sea environments or semi-enclosed coastal basins. This appeared to be the case within Saanich Inlet at 100 m depth during a 7-month eddy covariance study where Reimers et al. (2020) found average benthic fluxes of oxygen were only -1.6 ± 1.2 mmol m^{-2} d^{-1} despite organic-rich sediments.

The responses of fauna to hypoxia in Saanich Inlet and other well-studied eutrophic coastal fjords and basins have been observed to follow patterns of progressive behavioral changes and physiological stress, leading to population changes that favor more hypoxia-tolerant species as DO concentrations decrease to severely low levels (Levin et al. 2009; Matabos et al. 2012; Tunnicliffe et al. 2020). Manifestations of hypoxic stress in benthic organisms can include movement to the surface and out of sediments (Montagna and Ritter 2006) where they may benefit from turbulent and advective fluxes of DO. In our bottom imagery, we did not observe organisms that are normally found within the sediment residing on the surface. Since the sediments are permeable, bioturbated, and under strong flows and high turbulence, any threshold for emergence may not have occurred. Thus, reports of localized mortalities in assemblages of benthic invertebrates do appear to signal the onset of anoxia as inferred by Chan et al. (2008).

Richness per 0.1 m^2 box core in this study (11 to 28 taxa) was substantially lower than that observed in summer 2003 shelf assessments between 40 and 48°N (20-100; Henkel and Nelson 2018) but similar to summer assessments in 2010-12 (21-38; Henkel and Politano 2017), which mirrors the trends in dissolved oxygen observed in those studies (85-138 µmol L^{-1}, Henkel and Nelson 2018; 52-65 µmol L^{-1} Henkel and Politano unpublished data). However, the fewer taxa relative to collections in 2003 may reflect the myriad changes within the northern California

Current over the last two decades (Barth et al. 2024), not just deoxygenation trends. A multivariate analysis by Henkel and Politano (2017) of macrofaunal invertebrate groupings across the shelf from northern California to southern Washington at depths spanning 50 to 110 m found that assemblages correlated primarily with sediment texture (percent fines, and median grain size - spanning silt to gravel), and thus presumably with other wide-scale environmental factors that determine or depend on sediment grain size such as riverine inputs, currents, winter wave energy, and permeability, respectively (Voohries et al. 2018).

Bottom imagery confirmed all study sites were habitat for active infauna, often showing the burrow openings of the shrimp *Neotrypaea gigas,* which is an ecosystem engineer that can influence sediment characteristics, pore water chemistry, and benthic fluxes. *Neotrypaea gigas* were first found in high numbers with multiple cohorts on the central Oregon shelf in 2019 (Henkel et al. 2022). They were present in 45% of box cores across the four sites sampled in 2022, at densities up to 15 per box core or 150 m^{-2} (Table 1). These results indicate a sizeable offshore population contributing greater biomass and metabolism overall than other smaller taxa. The highest *in situ* oxygen concentration, *in situ* flux as measured by eddy covariance, and core incubation oxygen flux were measured at the site with the highest *Neotrypaea gigas* densities and the second highest density of burrow openings observed in the nearby seafloor video (NKW1). *Neotrypaea* sp. have been characterized as oxyregulators that increase ventilation behaviors to oxygenate their burrows and to resist hypoxic stress (Levia et al. 2015). They are also subsurface deposit feeders and, like other Callianassid burrowing shrimp, generally influence bioturbation via mixing and conveying of sediment during burrow formation and maintenance (Clare et al. 2022; Queirós et al. 2013).

The characteristic polychaetes observed in this study were similar at the three central Oregon sites, including the tube-dwelling *Spiophanes norrisi*, described as a surface depositor by Clare et al. (2022) and an upward and downward conveyor by Queirós et al. (2013), and *Leitoscoplos pugettensis,* which has been described as a common intertidal and subtidal burrower and deposit feeder (Hiebert 2015). Two of these sites also supported free-living predatory *Nephtys* sp. and burrow-dwelling subsurface deposit-feeding *Notomastus* sp., thus, with bottom images, collectively suggesting active bioturbation under hypoxic conditions that should contribute to sediment oxygen consumption. The more northern Oregon sites, NKW1 and NEH2, which exhibited the highest DO fluxes, were additionally characterized by suspension-feeding, tube-dwelling *Onuphis iridescens*. The densities of *O. iridescens* (average of 37-75 m^{-2}; Table 1) exceeded those reported for eastern U.S.A. tidal flat congeners*, O. microcephela* (average of 26 m^{-2}; Pryor 1975) and *O. jenneri* (8-79 m^{-2}; Waldbusser and Marinelli 2009) whose densities have been correlated to rates of pore water advection. The most abundant polychaete at the northern Oregon site NEH2 and the Washington WLP1 was the burrowing *Galathowenia* (prev. *Myriochele*) *oculata,* which is both a surface suspension and surface deposit feeder and considered a downward conveyor by Clare et al. (2022) but a surficial modifier by Queirós et al. (2013). On the western continental shelf of the U.K., *G. oculata* was the principal species defining similarity among grab samples from unconsolidated-sediment habitats, where the percent cover of bioturbated surface also made a significant contribution to habitat group similarities (McGonigle et al. 2009). Such observations suggest that *G. oculata* likely plays a role in surface modification on the Oregon-Washington shelf, adding to the creation of biological roughness.

494 The near-bottom velocity profiles measured at the NKW1, NEH2&1, and WLP1 sites
495 showed wave-current interactions, which can enhance bottom turbulence and feedback to reduce
496 hypoxic stress to the benthos. Velocity time series at all study sites also displayed the interacting
497 influences of surface waves, internal waves, and tides. Thus, the physical forces that drive
498 interfacial transport and carry DO to benthic communities act in conjunction with organic matter
499 fluxes, bioturbation, and particle trapping (Huettel and Rusch 2000) to sustain oxygen
500 consumption as a vigorous process over much of the Oregon-Washington middle shelf.
501 Latitudinal differences are evident in the groupings of species, indicating other regional
502 controlling factors such as shelf morphology or conditions that alter the seafloor during non-
503 summer seasons. Similar findings are very likely to be observed on other open, sediment-
504 covered, continental shelves. The variable dynamics create a complex interplay with the benthos,
505 which has not been fully recognized in shelf ecosystem and population studies or when
506 characterizing the effects of hypoxia. We advocate that, as a first advance, future studies
507 consider that it is the dynamics of the benthic oxygen supply that will shape benthic responses to
508 hypoxia, not simply the DO concentration.

Acknowledgements

This work was supported by a grant from the National Science Foundation to S. Henkel and C. Reimers [grant number OCE-2126112] and an earlier grant to C. Reimers [OCE-1634319]. Equipment acquired with funding from Oregon Sea Grant #NA18OAR4170072 (CFDA No. 11.417), Project number R/HBT-23-Reimers2022 was used for the collection of velocity profiles. We are grateful to the crews, marine technicians, and research assistants aboard R/Vs *Oceanus* and *Robert Gordon Sproul* for their contributions to operations and sampling. The manuscript benefited from reviews by Peter Berg and two anonymous reviewers.

Author Contribution Statement

All authors contributed to the field work and collection of data. Clare Reimers led the research cruises, analyzed the eddy covariance and velocity profile data, prepared figures and tables, and wrote the paper. Sarah Henkel directed the box coring and drop-camera collections, assembled the macrofauna analyses, and provided content for the paper's discussion. Waldo Wakefield provided the video beam trawl, identified fauna within images, and reviewed the text. Kristen Fogaren and Anna Hughes provided details and editing to the text.

Data Availability Statement

The data that support the findings of this study are available through the repository BCO-DMO.

DOI: 10.26008/1912/bco-dmo.962251.1

BCO-DMO Metadata Landing Page: https://www.bco-dmo.org/dataset/962251

References

Abelson, A., T. Miloh, and Y. Loya. 1993. Flow patterns induced by substrata and body morphologies of benthic organisms, and their roles in determining availability of food particles. *Limnology and Oceanography* **38**: 1116-1124. https://doi.org/10.4319/lo.1993.38.6.1116

Adams, K. A., J. A. Barth, and R. K. Shearman. 2016. Intraseasonal cross-shelf variability of hypoxia along the Newport, Oregon, Hydrographic Line. *Journal of Physical Oceanography* **46**: 2219-2238. https://doi.org/10.1175/JPO-D-15-0119.1

Attard, K. M., R. N. Glud, D. F. McGinnis, and S. Rysgaard. 2014. Seasonal rates of benthic primary production in a Greenland fjord measured by aquatic eddy correlation. *Limnology and Oceanography* **59**: 1555-1569. https://doi.org/10.4319/lo.2014.59.5.1555

Barth, J. A., S. D. Pierce, B. R. Carter, F. Chan, A. Y. Erofeev, J. L. Fisher, R. A. Feely, K. C. Jacobson, A. A. Keller, C. A. Morgan, J. E. Pohl, L. K. Rasmuson, and V. Simon. 2024. Widespread and increasing near-bottom hypoxia in the coastal ocean off the United States Pacific Northwest. *Nature Scientific Reports* **14**: 3798. https://doi.org/10.1038/s41598-024-54476-0

Berens, P. 2009. CircStat: A MATLAB Toolbox for Circular Statistics. *Journal of Statistical Software* **31**: 1-21. https://doi.org/10.18637/jss.v031.i10

Berg, P., M. Huettel, R. N. Glud, C. E. Reimers, and K. A. Attard. 2022. Aquatic eddy covariance: the method and its contributions to defining oxygen and carbon fluxes in marine environments. *Annual Review of Marine Science* **14**: 431-455. https://doi.org/10.1146/annurev-marine-042121-012329

Berg, P., H. Røy, F. Janssen, V. Meyer, and B. B. Jørgensen. 2003. Oxygen uptake by aquatic sediments measured with a novel non-invasive eddy-correlation technique. *Mar. Ecol. Prog. Ser.* **261**: 75 - 83.

Berg, P., H. Røy, and P. L. Wiberg. 2007. Eddy correlation flux measurements: The sediment surface area that contributes to the flux. *Limnology and Oceanography* **52**: 1672-1684. https://doi.org/10.4319/lo.2007.52.4.1672

Boland, G.S. and G.T. Rowe. 1991. Deep-sea benthic sampling with the GOMEX box corer. *Limnology and Oceanography* **36**: 1015-1020. https://doi.org/10.4319/lo.1991.36.5.1015

Boudreau, B. P. 1997. Diagenetic Models and Their Implementation. 417p. Springer-Verlag. ISBN-13:978-3-642-64399-6. https://doi.org/10.1 007/978-3-642-60421-8

Boudreau, B. P., and B. B. Jørgensen, (eds.). 2001. The Benthic Boundary Layer: Transport Processes and Biogeochemistry. Oxford Univ. Press. ISBN 0-19-511881-2. https://doi.org/10.1007/978-3-642-60421-8

574 Breitburg, D., L. A. Levin, A. Oschlies, M. Grégoire, F. P. Chavez, D. J. Conley, V. Garçon, D.
575 Gilbert, D. Gutiérrez, K. Isensee, G. S. Jacinto, K. E. Limburg, I. Montes, S. W. A. Naqvi, G. C.
576 Pitcher, N. N. Rabalais, M. R. Roman, K. A. Rose, B. A. Seibel, M. Telszewski, M. Yasuhra,
577 and J. Zhang. 2018. Declining oxygen in the global ocean and coastal waters. *Science* **359**: 7240.
578 https:/doi.org/10.1126/science.aam7240
579
580 Chan, F., J. A. Barth, J. Lubchenco, A. Kirincich, H. Weeks, W. T. Peterson, and B. A. Menge.
581 2008. Emergence of anoxia in the California current large marine ecosystem. *Science*
582 **319**: 920. https://doi.org/10.1126/science.1149016
583
584 Chriss, T. M., and D. R. Caldwell. 1982. Evidence for the influence of form drag on bottom
585 boundary layer flow. *Journal of Geophysical Research* **87**: 4148-4154.
586 https://doi.org/10.1029/JC087iC06p04148
587
588 Clare, D. S., S. G. Bolam, P. S. McIlwaine, C. Garcia, J. M. Murray, and J. D. Eggleton. 2022.
589 Biological traits of marine benthic invertebrates in Northwest Europe. *Scientific Data* **9**: 339.
590 https://doi.org/10.1038/s41597-022-01442-y
591
592 Clarke K. R. and R. N. Gorley. 2006. PRIMER v6: User Manual/Tutorial. PRIMER-E,
593 Plymouth.
594

595 Connolly, T. P., B. M. Hickey, S. L. Geier, and W. P. Cochlan. 2010. Processes influencing
596 seasonal hypoxia in the northern California Current System. *Journal of Geophysical Research*
597 **115**: C03021. https:/doi.org/10.1029/2009JC005283
598
599 Díaz, R. J., and R. Rosenberg. 2008. Spreading dead zones and consequences for marine
600 ecosystems. *Science* **321**: 926–929. https://doi.org/10.1126/science.1156401
601
602 Fennel, K., and J. M. Testa. 2019. Biogeochemical controls on coastal hypoxia. *Annual Review*
603 *of Marine Science* **11**: 103-130. https://doi.org/10.1146/annurev-marine-010318-095138
604
605 Fuchsman, C. A., A. H. Devol, Z. Chase, C.E. Reimers and B. Hales. 2015. Benthic fluxes on the
606 Oregon shelf. Estuarine, Coastal and Shelf Science, Part B 163: 156-166.
607 https://doi.org/10.1016/j.ecss.2015.06.001
608
609 Glud, R. N. 2008. Oxygen dynamics of marine sediments. *Marine Biology Research* **4**: 243-289.
610 https://doi.org/10.1080/17451000801888726
611
612 Goldfinger, C., S. K. Henkel, C. Romsos, A. Havron, and B. Black. 2014. Benthic habitat
613 characterization offshore the Pacific Northwest. Volume 1: Evaluation of Continental Shelf
614 Geology. US Dept. of the Interior, Bureau of Ocean Energy Management, Pacific OCS Region.
615 OCS Study BOEM 2014-662. 161 pp.
616

617 Henkel, S. K. and L. A. Gilbane. 2020. Using benthic macrofaunal assemblages to define habitat
618 types on the northeast Pacific sedimentary shelf and slope. *Estuarine Coastal and Shelf Science*
619 **246**: 107056. https://doi.org/10.1016/j.ecss.2020.107056
620
621 Henkel, S, K. and W. G. Nelson. 2018. Assessment of spatial patterns in benthic macrofauna of
622 the U.S. west coast continental shelf. *Journal of Biogeography* **45**: 2701-2717.
623 https://doi.org/10.1111/jbi.13451
624
625 Henkel, S. K. and K. K. Politano. 2017. Small proportions of silt linked to distinct and
626 predictable differences in marine macrofaunal assemblages on the continental shelf of the Pacific
627 Northwest. *Continental Shelf Research* **144**: 38-49. https://doi.org/10.1016/j.csr.2017.06.016
628
629 Henkel, S. K., E.C. Revelas, S. Wodzicki, and J. Chapman. 2022. Discovery of a large offshore
630 population of the northeast Pacific burrowing shrimp *Neotrypaea* sp. (Decapoda: Axiidea).
631 *Estuarine, Coastal and Shelf Science* **274**: 107936. https://doi.org/10.1016/j.ecss.2022.107936
632
633 Hiebert, T. C. 2015. *Leitoscoloplos pugettensis*. In: Oregon Estuarine Invertebrates: Rudys'
634 Illustrated Guide to Common Species, 3rd ed. T. C. Hiebert, B. A. Butler and A. L. Shanks
635 (eds.). University of Oregon Libraries and Oregon Institute of Marine Biology, Charleston, OR.
636
637 Hoffman, F., H. Røy, K. Bayer, U. Hentschel, M. Pfannkuchen, F. Brümmer, and D. de Beer.
638 2008. Oxygen dynamics and transport in the Mediterranean sponge *Aplysina aerophoba. Marine*
639 *Biology* **153**: 1257-1264. https://doi.org/10.1007/s00227-008-0905-3

Holtappels, M., R. N. Glud, D. Donis, B. Liu, A. Hume, F. Wenzhöfer, and M. M. M. Kuypers . 2013. Effect of transient bottom water currents and oxygen concentrations on benthic exchange rates as assessed by eddy correlation measurements. *Journal of Geophysical Research-Oceans* **118**: 1157–1169. https://doi.org/10.1002/jgrc.20112

Huettel, M., P. Berg, and A. Merikhi. 2020. Technical note: Measurements and data analysis of sediment-water oxygen flux using a new dual-optode eddy covariance instrument. *Biogeosciences* **17**: 4459-4476. https://doi.org/10.5194/bg-17-4459-2020

Huettel, M. and A. Rusch. 2000. Transport and degradation of phytoplankton in permeable sediment. *Limnology and Oceanography* **45**: 534-549. https://doi.org/10.4319/lo.2000.45.3.0534

Hughes, A., C. E. Reimers, K. E. Fogaren, and Y. Alleau. 2025. Spatiotemporal variability in benthic-pelagic coupling on the Oregon-Washington shelf. *Marine Chemistry* **268**: 104473. https://doi.org/10.1016/j.marchem.2024.104473

Jarvis, B. M., R. M. Greene, Y. Wan, J. C. Lehrter, L. L. Lowe, and D. S. Ko. 2021. Contiguous low oxygen waters between the continental shelf hypoxia zone and nearshore coastal waters of Louisiana, USA: Interpreting 30 years of profiling data and three-dimensional ecosystem modeling. *Environmental Science and Technology* **55**: 4709-4719. https://doi.org/10.1021/acs.est.0c05973

663 Jørgensen, B. B., F. Wenzhöfer, M. Egger, and R. N. Glud. 2022. Sediment oxygen
664 consumption: Role in the global marine carbon cycle. *Earth-Science Reviews* **228**: 103987.
665
666 Keller, A.A., L. Ciannelli, W.W. Wakefield, V. Simon, J.A. Barth, and S.D. Pierce. 2015.
667 Occurrence of demersal fishes in relation to near-bottom oxygen levels within the California
668 Current large marine ecosystem. *Fisheries Oceanography* **24**: 162-176.
669 https://doi.org/10.1111/fog.12100
670
671 Keller, A. A., V. Simon, F. Chan, W. W. Wakefield, M. E. Clarke, J. A. Barth, D. Kamikawa and
672 E. L. Fruh. 2010. Demersal fish and invertebrate biomass in relation to an offshore hypoxic zone
673 along the US West Coast. *Fisheries Oceanography* **19**: 76-87. https://doi.org/10.1111/j.1365-
674 2419.2009.00529.x
675
676 Komar, P. D., R. H. Neudeck, and L. D. Kulm. 1972. Observations and significance of deep-
677 water oscillatory ripple marks on the Oregon continental shelf, in Swift D. J. P., Duane D. B.,
678 and Pilkey O. H. eds. Shelf Sediment Transport. Stroudsburg, Pennsylvania, Dowden,
679 Hutchinson and Ross, Inc.: 601-619.
680
681 Kravitz, M., W. G. Pearcy, and M. P. Gum. 1977. Food of five species of cooccurring flatfishes
682 on Oregon's continental shelf. *Fishery Bulletin* **74**: 984-990.
683

Kulm, L. D., R. C. Boush, J. C. Harlett, R. H. Neudeck, D. M. Chambers, and E. J. Runge. 1975. Oregon continental shelf sedimentation: interrelationships of facies distributions and sedimentary processes. *The Journal of Geology* **83**: 145-175.

Lee, Y., E. Byeon, D.-H. Kim, P. Maszczyk, M. Wang, R. S. S. Wu, H.-D. Jeung, U.-K. Hwang, and J.-S. Lee. 2023. Hypoxia in aquatic invertebrates: Occurrence and phenotypic and molecular responses. *Aquatic Toxicology* **263**: 106685. https://doi.org/10.1016/j.aquatox.2023.106685

Leiva, F.P., M.A. Urbina, J.P. Cumillaf, P. Gebauer, and K. Paschle. 2015. Physiological responses of the ghost shrimp *Neotrypaea uncinata* (Milne Edwards 1837) (Decapoda: Thalassinidea) to oxygen availability and recovery after severe environmental hypoxia. *Comparative Biochemistry and Physiology* **189**: 30-37. https://doi.org/10.1016/j.cbpa.2015.07.008

Levin, L. A., W. Ekau, A. J. Gooday, F. Jorissen, J. J. Middelburg, S. W. A. Naqvi, C. Neira, N. N. Rabalais, and J. Zhang. 2009. Effects of natural and human-induced hypoxia on coastal benthos. *Biogeosciences* **6**: 2063-2098. https://doi.org/10.5194/bg-6-2063-2009

Matabos, M., V. Tunnicliffe, S. Juniper, and C. Dean. 2012. A year in hypoxia: Epibenthic community responses to severe oxygen deficit at a subsea observatory in a coastal inlet. *PLoS ONE* **7**: e45626. https//doi.org/10.1371/journal.pone.0045626

McCann-Grosvenor, K., C. E. Reimers, and R. D. Sanders. 2014. Dynamics of the benthic boundary layer and seafloor contributions to oxygen depletion on the Oregon inner shelf. *Continental Shelf Research* **84**: 93-106. https://doi.org/10.1016/j.csr.2014.05.010

McGonigle, C., C. Brown, R. Quinn, and J. Grabowski. 2009. Evaluation of image-based multibeam sonar backscatter classification for benthic habitat discrimination and mapping at Stanton Banks, UK. *Estuarine, Coastal and Shelf Science* **81**:423–437. https://doi.org/10.1016/j.ecss.2008.11.017

Montagna, P. A. and C. Ritter. 2006. Direct and indirect effects of hypoxia on benthos in Corpus Christi Bay, Texas, U.S.A. *Journal of Experimental Marine Biology and Ecology* **330**: 119-131. https://doi.org/10.1016/j.jembe.2005.12.021

Moum, J., J. M. Klymak, J. D. Nash, A. Perlin, and W. D. Smyth. 2007. Energy transport by nonlinear internal waves. *Journal of Physical Oceanography* **37**: 1968-1988. https://doi.org/10.1175/JPO3094.1

Pearcy, W. G. and D. Hancock. 1978. Feeding habits of Dover sole, *Microstomus pacificus*; rex sole, *Glyptocephalus zachirus*; slender sole, *Lyopsetta exilis*; and Pacific sanddab, *Citharichthys sordidus*, in a region of diverse sediments and bathymetry off Oregon. *Fishery Bulletin* **75**:173-183.

728 Perlin, A., J. N. Moum, and J. M. Klymak. 2005. Response of the bottom boundary layer over a
729 sloping shelf to variations in alongshore wind. *Journal of Geophysical Research* **110**: C10S09.
730 https//doi.org/10.1029/2004JC002500
731
732 Perry, S. F., M. Lambertz, and A. Schmitz. 2019. Respiratory faculties of aquatic invertebrates.
733 In: *Respiratory Biology of Animals: Evolutionary and Functional Morphology.* Oxford
734 University Press. https://doi.org/10.1093/oso/9780199238460.001.0001
735
736 Pierce, S. D., J. A. Barth, K. Shearman, and A. Y. Erofeev. 2012. Declining oxygen in the
737 Northeast Pacific. *Journal of Physical Oceanography* **42**: 495-501. https://doi.org/10.1175/JPO-
738 D-11-0170.1
739
740 Pryor, W. A. 1975. Biogenic sedimentation and alteration of argillaceous sediments in shallow
741 marine environments. *Geological Society of America Bulletin* **86**: 1244-1254.
742 https://doi.org/10.1130/0016-7606(1975)86%3C1244:BSAAOA%3E2.0.CO;2
743
744 Queirós, A. M., S. N. Birchenough, J. Bremner, J. A. Godbold, R. E. Parker, A. Romero-
745 Ramirez, H. Reiss, M. Solan, P. J. Somerfield, C. Van Colen, and G. Van Hoey. 2013. A
746 bioturbation classification of European marine infaunal invertebrates. *Ecology and Evolution* **3**:
747 3958-3985. https://doi.org/10.1002/ece3.769
748

Rabalais, N. N., R. J. Díaz, L. A. Levin, R. E. Turner, D. Gilbert, and J. Zhang. 2010. Dynamics and distribution of natural and human-caused hypoxia. *Biogeosciences* **7**: 585-619. https://doi.org/10.5194/bg-7-585-2010

Rabalais, N. N., R. E. Turner, and W. J. Wiseman. 2002. Gulf of Mexico hypoxia, aka ‘‘The dead zone’’. *Annual Review of Ecology, Evolution, and Systematics* **33**: 235–263. https://doi.org/10.1146/annurev.ecolsys.33.010802.150513

Reimers, C..E. and K. E. Fogaren. 2021. Bottom boundary layer oxygen fluxes during winter on the Oregon shelf. *Journal of Geophysical Research-Oceans* **126**: e2020JC016828. https://doi.org/10.1029/2020JC016828

Reimers, C. E., H. T. Özkan-Haller, R. D. Sanders, K. McCann-Grosvenor, K., P. J. Chace, and S. A. Crowe. 2016. The dynamics of benthic respiration at a mid-shelf station off Oregon. *Aquatic Geochemistry* **22**: 505-527. https://doi.org/10.1007/s10498-016-9303-5

Reimers, C. E., H. T. Özkan-Haller, P. Berg, A. Devol, K. McCann-Grosvenor, and R. D. Sanders. 2012. Benthic oxygen consumption rates during hypoxic conditions on the Oregon continental shelf: Evaluation of the eddy correlation method. *Journal of Geophysical Research-Oceans* **117**: C02021, https//doi.org/10.1029/2011JC007564

Reimers, C. E., R. D. Sanders, R. Dewey, and R. Noel. 2020. Benthic fluxes of oxygen and heat from a seasonally hypoxic region of Saanich Inlet fjord observed by eddy covariance. *Estuarine, Coastal and Shelf Science* **243**: 106815. https//doi.org/10.1016/j.ecss.2020.106815

Risien, C. M., B. T. Cervantes, M. R. Fewings, J. A. Barth and P. M. Kosro. 2023. A stitch in time: Combining more than two decades of mooring data from the central Oregon shelf. *Data in Brief* **48**: 109041. https://doi.org/10.1016/j.dib.2023.109041

Siedlecki, S. A., N. S. Banas, K. A. Davis, S. Giddings, S., B. M. Hickey, P. MacCready, T. Connolly, T. and S. Geier. 2015. Seasonal and interannual oxygen variability on the Washington and Oregon continental shelves. *Journal of Geophysical Research-Oceans* **120**: 608-633. https://doi.org/10.1002/2014JC010254

Shapiro, O. H., V. I. Fernando, M. Garren, and R. Stocker. 2014. Vortical ciliary flows actively enhance mass transport in reef corals. *Proceedings of the National Academy of Sciences* **111**: 13391-13396. https://doi.org/10.1073/pnas.1323094111

Somero, G. N., J. M. Beers, F. Chan, T. A. Hill, T. Klinger, and S. Y. Litvin. 2016. What changes in carbonate system, oxygen, and temperature portend for the Northeastern Pacific Ocean: A physiological perspective. *BioScience* **66**: 14-26. https://doi.org/10.1093/biosci/biv162

Stinton, A., L. Ciannelli, D. C. Reese, and W. W. Wakefield. 2014. Using in situ video analysis to assess juvenile flatfish behavior along the Oregon Central Coast. *CalCOFI Reports* **55**: 158-168.

Storch, V. and G. Alberti. 1978. Ultrastructural observations on the gills of polychaetes. *Helgoländer wissenschaftliche Meeresuntersuchungen* **31**: 169-179.

Trowbridge, J. H. and Y. C. Agrawal. 1995. Glimpses of a wave boundary layer. *Journal of Geophysical Research-Oceans* **100**: 20,729-20,743. https://doi.org/10.1029/95JC02131

Trowbridge, J. H. and S. J. Lentz. 1998. Dynamics of the bottom boundary layer on the northern California shelf. *Journal of Physical Oceanography* **28**: 2075–2093. https://doi.org/10.1175/1520-0485(1998)028<2075:DOTBBL>2.0.CO;2

Trowbridge, J. H. and S. J. Lentz. 2018. The bottom boundary layer. *Annual Review of Marine Science* **10**: 397-420. https://doi.org/10.1146/annurev-marine-121916-063351

Tunnicliffe, V., R. Gasbarro, F. Juanes, J. Qualley, N. Soderberg, and J. W. F. Chu. 2020. An hypoxia-tolerant flatfish: consequences of sustained stress on the slender sole *Lyopsetta exilis* (Pleuronectidae) in the context of a changing ocean. *Journal of Fish Biology* **96**: 394-407. https//doi.org/10.1111/jfb.14212

Vaquer-Sunyer, R., and C. M. Duarte. 2008. Thresholds of hypoxia for marine biodiversity. *Proceedings of the National Academy of Sciences* **105**: 15452-15457. https//doi.org/10.1073/pnas.0803833105

Voorhies, K.J., Wootton, J.T., Henkel, S.K., 2018. Longstanding signals of marine community structuring by winter storm wave-base. *Marine Ecology Progress Series* **603**: 135–146. https//doi.org/10.3354/ meps12703

Waldbusser, G. G. and R. L. Marinelli. 2009. Evidence of infaunal effects on porewater advection and biogeochemistry in permeable sediments: A proposed infaunal functional group framework. *Journal of Marine Research* **67**: 503-532.

Walter, R. K., S. A. Huie, J. C. P. Abraham, A. Pasulka, K. A. Davis, T. P. Connolly, P. L. F. Mazzini, and I. Robbins. 2022. Seasonal controls on nearshore dissolved oxygen variability and hypoxia in a coastal embayment. *Estuarine, Coastal and Shelf Science* **278**: 108123. https://doi.org/10.1016/j.ecss.2022.108123

Table 1. Average macrofaunal abundance and richness (per 0.1 m^2 box core), densities of the top characteristic invertebrate species within each taxonomic group, and average numbers of *Neotrypaea gigas* burrows m^{-2} in dual images from each of two video camera frame landings within each area of study. The bolded value is for the video images closest to the EC deployment location. n.d.=not determined.

Sampling area	**NH Line**	**PWS2**	**NKW1**	**NEH2**	**WLP1**
Number box cores	6	6	7	7	8
Water depths (m)	72-78	72-84	64-71	73-78	68-75
Average abundance per 0.1 m^{-2}	55	31	68	113	47
Average richness per 0.1 m^2	20	11	20	28	19
Characteristic Crustaceans (abundance per 0.1 m^2 box core)	*Ampelisca agassizi* (1.75) *Diastylopsis dawsoni* (1.00)	*Neotrypaea* sp. (0.92) *Diastylopsis dawsoni* (1.00)	*Neotrypaea* sp. (3.71) *Diastylopsis dawsoni* (2.14) *Rhepoxynius fatigans* (2.57) *& R. abronius* (1.43)	*Euphilomedes carcharodonta* (6.00) *Rhepoxynius fatigans* (2.57) *Diastylopsis dawsoni* (1.00) *Neotrypaea* sp. (0.29)	*Neotrypaea* sp. (1.43) *Diastylopsis dawsoni* (1.14)
Characteristic Molluscs (abundance per 0.1 m^2 box core)	*Alia gausapata* (22.00) *Axinopsida serricata* (4.00)	*Axinopsida serricata* (1.33) *Alia gausapata* (0.67) *Cylichna attonsa* (1.00)	*Kurtiella tumida* (25.57) *Acila castrensis* (4.71) *Cylichna attonsa* (1.57)	*Acila castrensis* (12.29) *Axinopsida serricata* (7.00) *Alia gausapata* (1.86)	*Nuculana hamata* (0.71) *Compsomyax subdiaphana* (0.86) *Pulsellum salishorum* (0.43)
Characteristic Polychaetes (abundance per 0.1 m^2 box core)	*Spiophanes norrisi* (10.75) *Nephtys* sp. (3.00)	*Leitoscoplos pugettensis* (1.83) *Notomastus* sp. (3.22)	*Onuphis iridescens* (3.72) *Leitoscoplos pugettensis* (2.48)	*Galathowenia oculata* (13.06) *Notomastus* sp. (6.94)	*Galathowenia oculata* (5.25) *Magelona longicornis* (4.38)

	Leitoscoplos pugettensis (2.00) *Notomastus* sp. (5.25)	*Nephtys* sp. (1.78) *Spiophanes norrisi* (3.94)	*Spiophanes norrisi* (2.64)	*Onuphis iridescens* (7.50) *Nephtys* sp. (1.38)	*Maldane sarsi* (2.25)
Characteristic Echinoderms (abundance per 0.1 m^2 box core)	None	None	*Amphiodia urtica* (1.00)	*Amphiodia urtica* (5.66) *Amphiodia occidentalis* (1.63)	*Amphiodia urtica* (7.88) *Amphiodia occidentalis* (0.88)
***Neotrypaea gigas* burrow densities per m^2**	n.d.	0, **24.4**	**11.9**, 2.5	82.5, **1.9**	**8.2**, 11.25

Table 2. Situational information for the eddy covariance (EC) data series and oxygen fluxes (mean ± 1 std dev) determined by eddy covariance methods and by core incubations.

EC Deployment number & site[+]	Start date (mm/dd/yy)	Duration (h)	Water depth (m)[*]	DO (μmol L^{-1})[†]	Temperature (^{o}C)	EC oxygen flux (mmol m^{-2} d^{-1})	% Record utilized[#]	Core incubation oxygen flux (mmol m^{-2} d^{-1})	Number of cores
1 NH80	07/03/18	24	81.7±0.6	46.7±2.3	7.51±0.01	-3.5±2.9	98.4	-1.2±1.5	2
2 NH80	07/03/18	24	80.4±0.6	48.6±2.9	nd	-3.7±2.9	93.8	--	--
3 NH80	08/02/18	27.5	82.2±0.5	46.3±0.8	7.61±0.01	-4.0±2.4	100	--	--
4 PWS2	07/22/22	29.75	84.1±0.6	24.7±1.2	7.53±0.02	-4.9±2.3	90.8	-1.3	1
5 NKW1	09/14/22	18.5	67.7±0.7	75.3±6.9	8.04±0.03	-23.0±11.2	95.8	-4.3±0.9	2
6 NEH2	09/15/22	22.5	75.2±0.6	41.0±6.0 41.3±5.8	8.00±0.05	-13.2±6.9 -13.3±9.3	97.5 95.9	-3.2±0.1	2
7 WLP1	09/16/22	31.5	71.1±0.6	17.0±2.9	7.82±0.02	-4.7±2.6	95.8	-2.3±0.1	2

[+]Deployments were made from R/V *Oceanus* during cruises OC1807A and OC1808A, and from R/V *Robert Gordon Sproul* during cruises SP2215 and SP2219; Lat./Long. #1-#7: 44.636 -124.308, 44.637 -124.313, 44.641 -124.307, 44.571 -124.304, 45.104 -124.072, 45.722 -124.067, 46.450 -124.305.

*Depth derived from the standard gravity variation with latitude and pressure using the mean and standard deviation of the Vector pressure record with the height of the pressure sensor added.

†Mean and standard deviation as assessed by the cross-calibrated fiber optic oxygen sensors. Where paired sensors were used, determinations from both are given.

[#]See supporting information for explanation of criteria for excluding data.

Table 3. Friction velocities and roughness lengths derived using logarithmic regression across flow speeds measured within the five lowest profile bins displayed in Fig. 7. Wave periods and wave heights were derived from simultaneous pressure recordings. The ranges of friction velocities calculated from Eq. 3 and ADV velocities from the same sites are reported as $EC\ u_*$ values.

Site	**Start DateTime** **MM/DD/YY** **hh:mm:ss**	**Record duration (min)**	u_* **(cm s^{-1})**	z_o **(cm)**	R^2	T_p **(s)**	H_s **(m)**	**Mean water depth (m)**	$EC\ u_*$ **(cm s^{-1})**
NKW1	9/14/22 21:47:00	4	0.71	1.4	0.98	15.0	0.40	67.1	0.18-1.16
NEH2	9/16/22 13:23:45	2	0.45	<0.1	0.70	13.3	0.71	77.2	0.05-0.78
WLP1	09/17/22 10:16:30	4	0.45	0.3	0.97	13.3	0.51	71.4	0.10-0.86
NEH1	09/18/22 16:08:30	5	0.57	2.0	0.99	9.1	1.1	60.9	n.d.

Figure Captions

Fig. 1. Regional bathymetry map of the seafloor off southern Washington and northern Oregon, USA, showing the principal study site locations. Surrounding seafloor images were taken contemporaneously with other measurements during this study. Laser beam spots in NH80 images are separated by 10 cm. Identifiable fauna and features include: Dungeness crab (NEH2), slender sole *Lyopsetta exilis* (PWS2), *Neotrypaea gigas* burrows (NKW1, WLP1, PWS2), helically coiled gastropods (NH80, NEH2, PWS2). One additional station from which limited data is reported (NEH1) is 3 km shoreward of NEH2 (see Hughes et al. 2025).

Fig. 2. Water column profiles of DO and seawater density determined from CTD casts at each study site within the time periods of the eddy covariance instrument deployments. Hypoxic waters are indicated by the shading.

Fig. 3. Time series of eddy covariance sensor measurements at NH80 in (**a**) July 2018 (deployment 1) and (**b**) August 2018 (deployment 3). Top panels show velocities in ENU Cartesian coordinates and mean horizontal speed for each 15-min segment. Middle panels show the ADV pressure record and dissolved oxygen at 8 Hz. Bottom panels display derived oxygen fluxes every 15 minutes.

Fig. 4. Comparison of flow characteristics during concurrent eddy covariance measurements by two separate systems during deployments 1 and 2 (designated as D1 and D2) at NH80 in July 2018. Each point represents 15-min representations of: (**a**) horizontal flow speed, and (**b**) friction velocity.

Fig. 5. Time series of eddy covariance sensor measurements at NEH2 (deployment 6). During this deployment, two oxygen sensors were used, yielding two oxygen time series (ox1 and ox2)

in the middle panel and two corresponding flux estimates for each 15-minute segment of the record in the bottom panel.

Fig. 6. Box and whisker plots showing Pearson correlation coefficients between rates of sediment oxygen consumption and parameters related to flow and DO conditions. The *r* values for individual deployments are indicated by the deployment number placement within each range (Min-Max). For deployment 6 at NEH2, the results with sensor ox1 were used.

Fig. 7. Snap-shot velocity profiles in East and North directions and corresponding profiles of horizontal flow speed at stations NKW1, NEH2, WLP1, and NEH1 (3 km shoreward of NEH2). Logarithmic model fits to the bottom 5 depth bins are plotted as dashed lines extended towards the seabed (0 height).


NEH2
73.6 m
8.8 °C

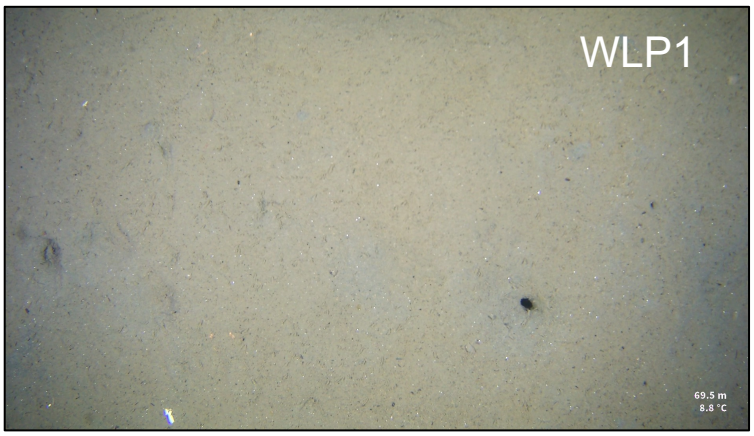
WLP1
69.5 m
8.8 °C

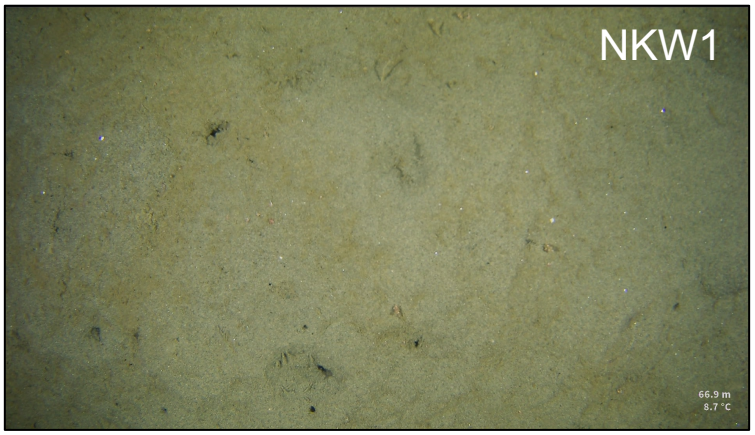
NKW1
66.9 m
8.7 °C

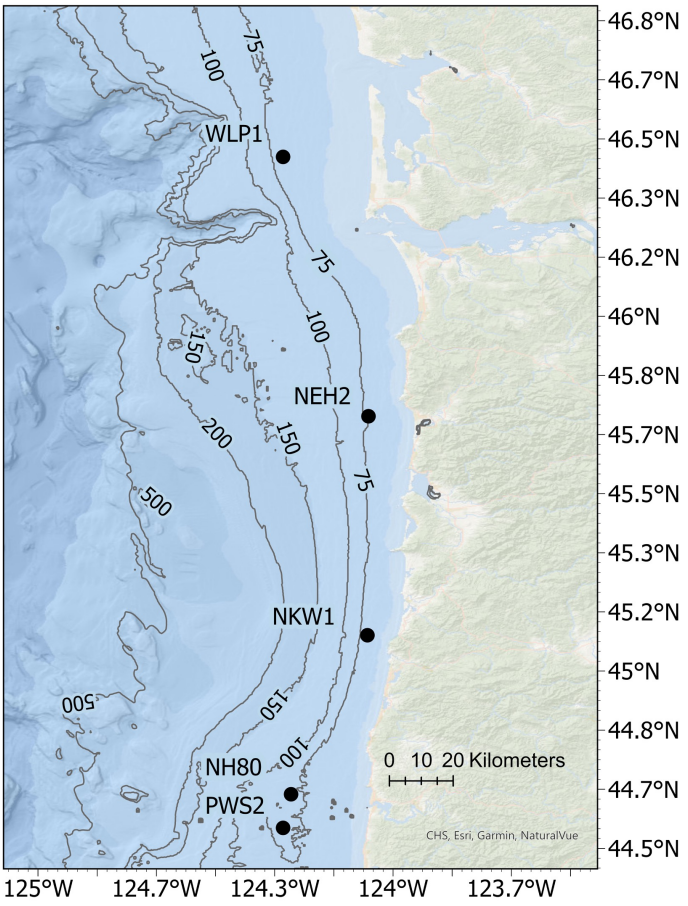
WLP1
NEH2
NKW1
NH80
PWS2
75
100
150
200
500
0 10 20 Kilometers
CHS, Esri, Garmin, NaturalVue
46.8°N
46.7°N
46.5°N
46.3°N
46.2°N
46°N
45.8°N
45.7°N
45.5°N
45.3°N
45.2°N
45°N
44.8°N
44.7°N
44.5°N
125°W
124.7°W
124.3°W
124°W
123.7°W

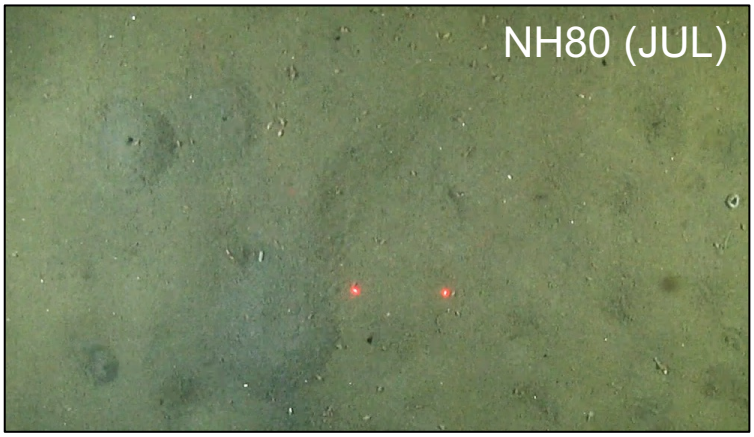
NH80 (JUL)

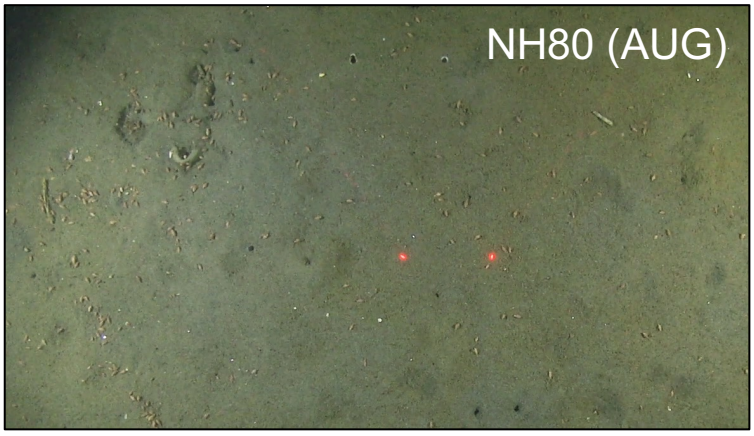
NH80 (AUG)


PWS2
83.1 m
8.4 °C

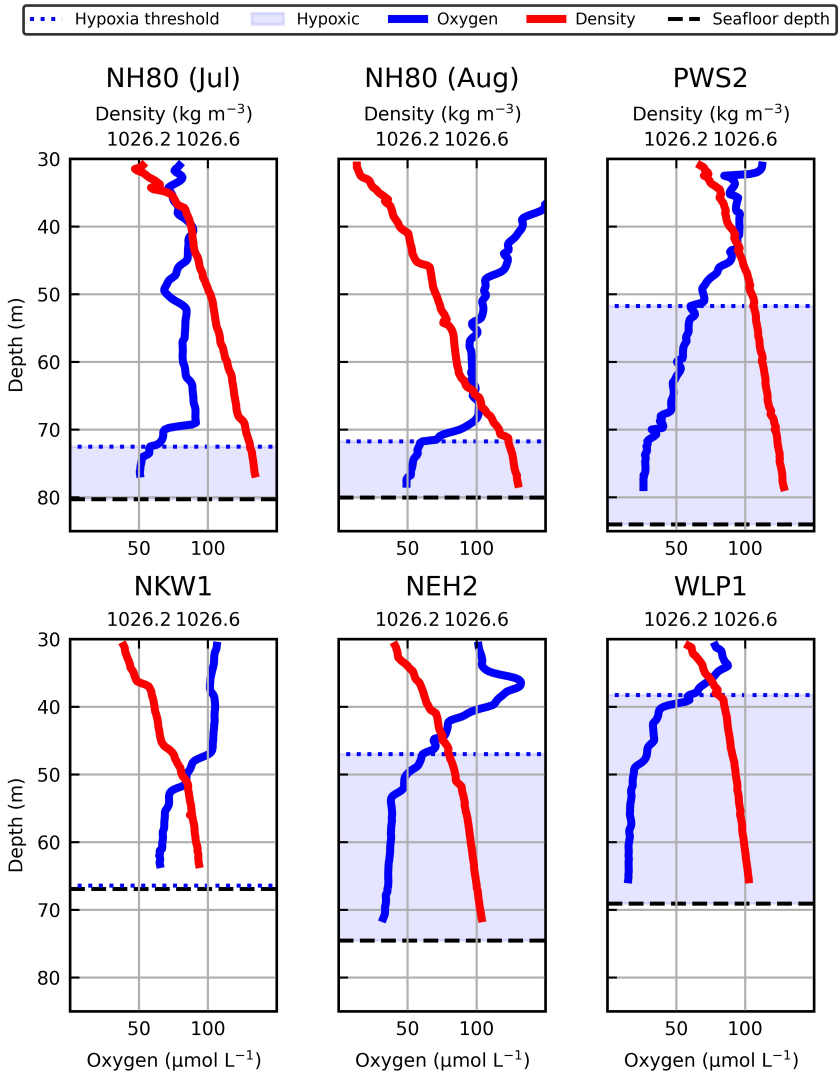
Hypoxia threshold
Hypoxic
Oxygen
Density
Seafloor depth
NH80 (Jul)
NH80 (Aug)
PWS2
NKW1
NEH2
WLP1
Density (kg m^{-3})
1026.2 1026.6
Depth (m)
30
40
50
60
70
80
50
100
Oxygen (µmol L^{-1})

(a)

NH80 July 3-4, 2018

Velocity (cm s^{-1})

E N U speed

Pressure (dbar)

pres ox

Oxygen (μmol L^{-1})

Oxygen flux (mmol m^{-2} d^{-1})

18:00 21:00 00:00 03:00 06:00 09:00 12:00 15:00

Local time (HH:MM)

(b)

NH80 August 2-3, 2018

Velocity (cm s^{-1})

E N U speed

Pressure (dbar)

pres ox

Oxygen (μmol L^{-1})

Oxygen flux (mmol m^{-2} d^{-1})

15:00 18:00 21:00 00:00 03:00 06:00 09:00 12:00 15:00

Local time (HH:MM)

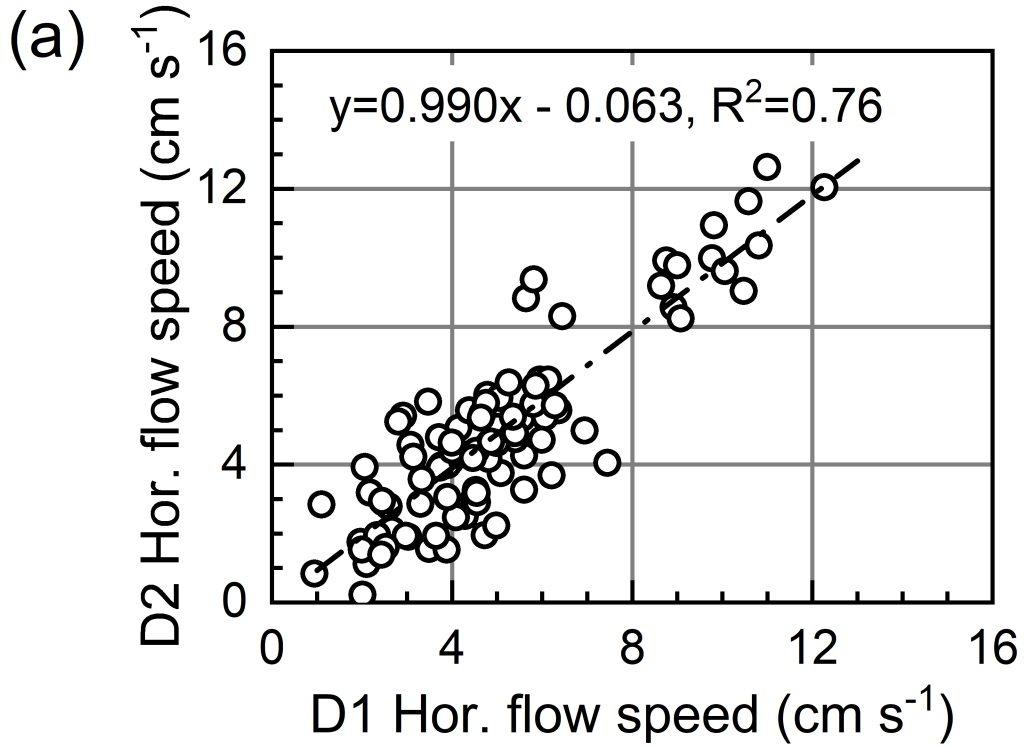
(a)
y=0.990x - 0.063, R2=0.76
D2 Hor. flow speed (cm s-1)
D1 Hor. flow speed (cm s-1)
0
4
8
12
16

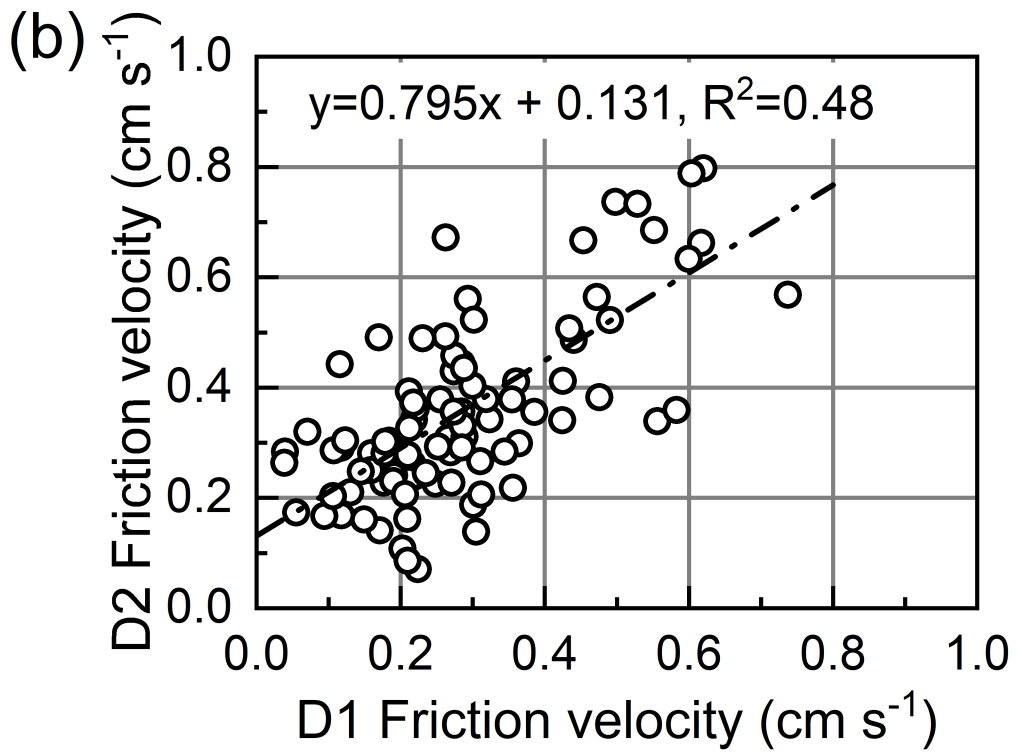
(b)
y=0.795x + 0.131, R2=0.48
D2 Friction velocity (cm s-1)
D1 Friction velocity (cm s-1)
0.0
0.2
0.4
0.6
0.8
1.0

NEH2 September 15-16, 2022

Velocity (cm s^{-1})

30
15
0
-15
-30

E
N
U
speed

Pressure (dbar)

78
77
76
75
74
73

pres
ox1
ox2

Oxygen (μmol L^{-1})

70
60
50
40
30
20

Oxygen flux (mmol m^{-2} d^{-1})

0
-20
-40

ox1
ox2

18:00
21:00
00:00
03:00
06:00
09:00
12:00
15:00

Local time (HH:MM)

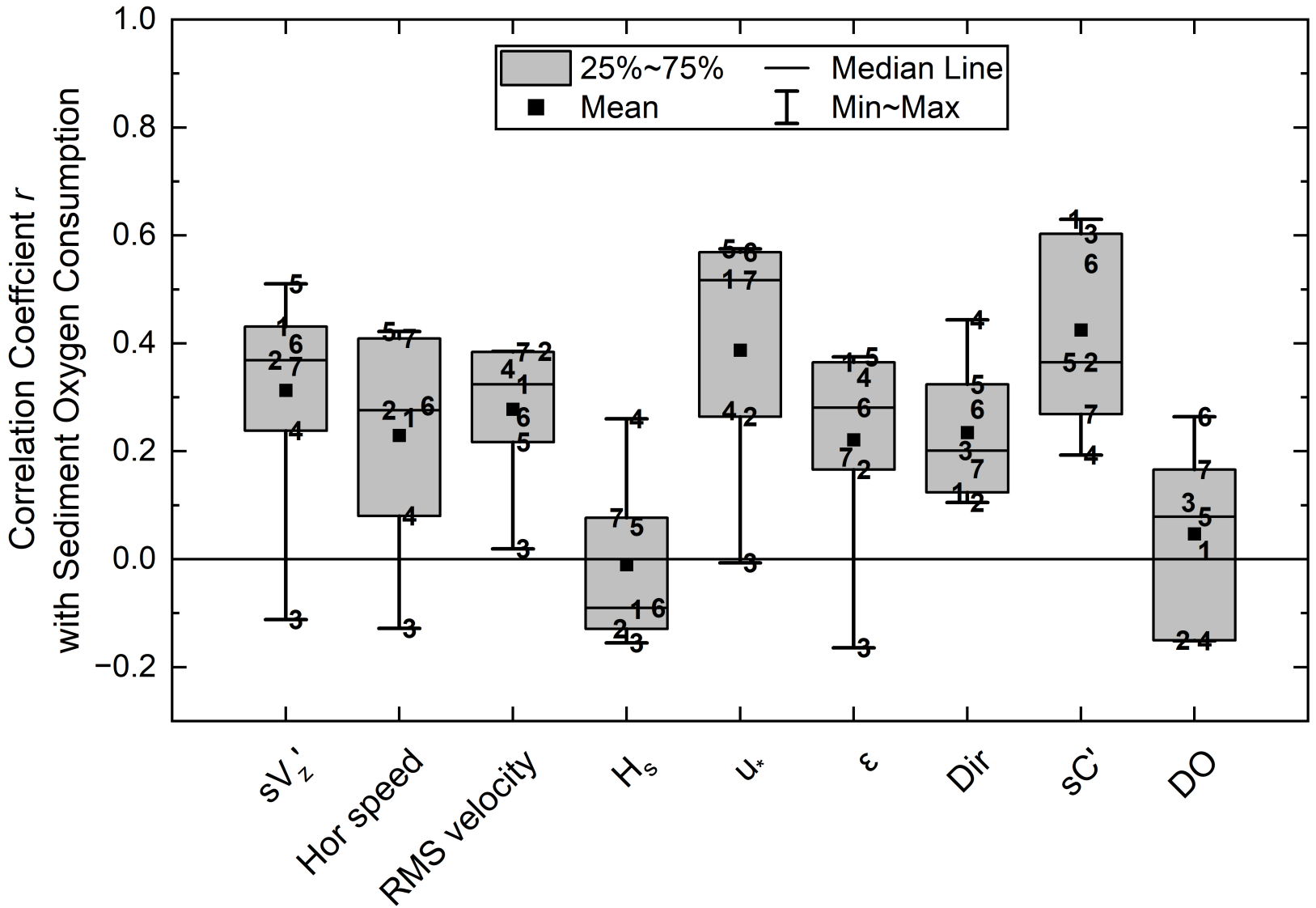
25%~75%
Median Line
Mean
Min~Max
Correlation Coeffcient r
with Sediment Oxygen Consumption
1.0
0.8
0.6
0.4
0.2
0.0
−0.2
sV'z
Hor speed
RMS velocity
Hs
u*
ε
Dir
sC'
DO

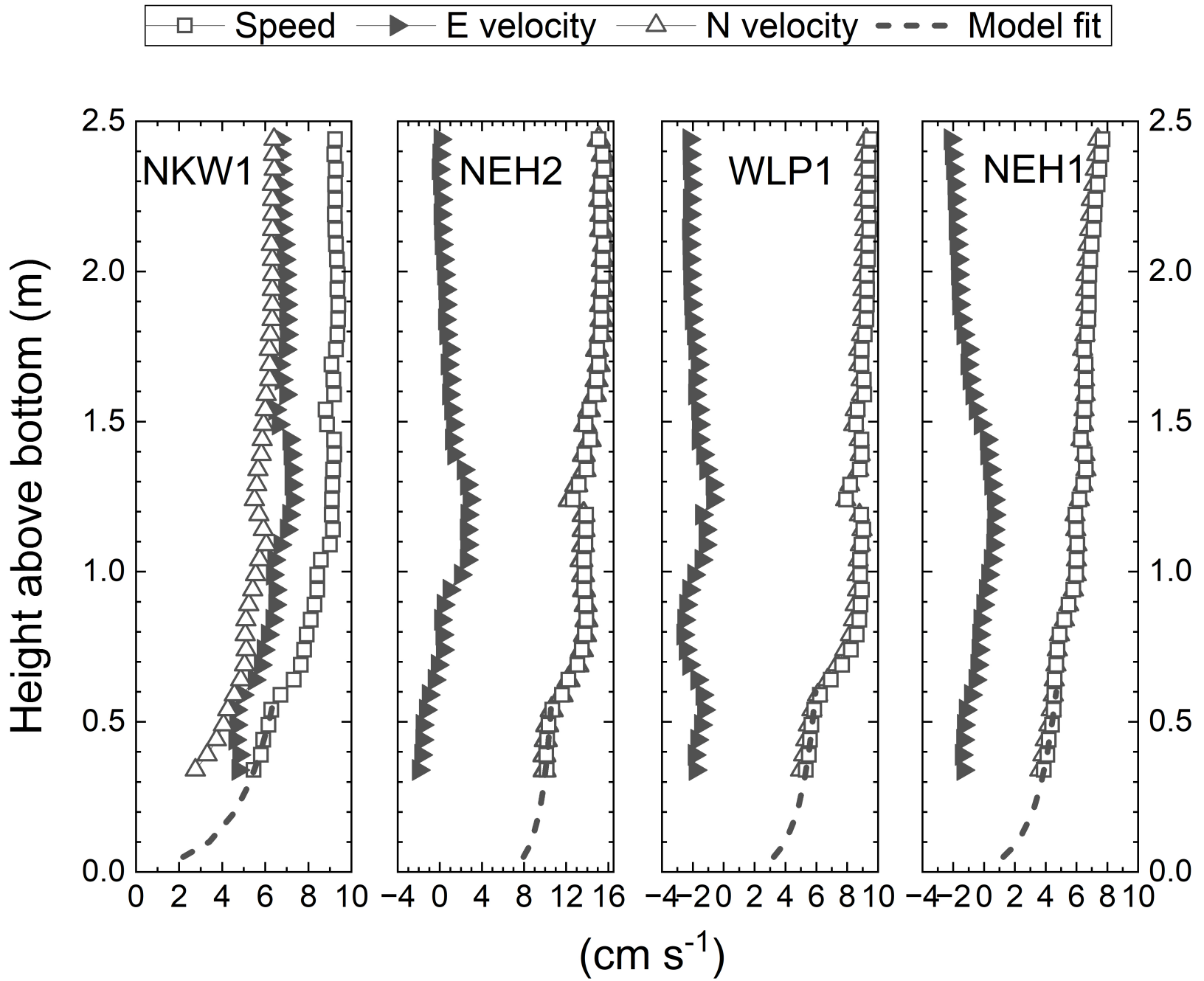
Speed
E velocity
N velocity
Model fit
NKW1
NEH2
WLP1
NEH1
Height above bottom (m)
0.0
0.5
1.0
1.5
2.0
2.5
0 2 4 6 8 10
−4 0 4 8 12 16
−4 −2 0 2 4 6 8 10
−4 −2 0 2 4 6 8 10
(cm s-1)

Supporting Information for

Dynamic Benthic Oxygen Fluxes Lessen Hypoxia Effects on Open Continental Shelves

Clare E. Reimers[1*], Sarah K. Henkel[2], Kristen E. Fogaren[1,3], Peter J. Chace[1], Anna Hughes[1] and W. Waldo Wakefield[4]

[1]College of Earth, Ocean, and Atmospheric Sciences, Oregon State University, Corvallis, Oregon, 97331, USA

[2]Department of Integrative Biology, Oregon State University, Corvallis, Oregon, 97331, USA

[3] Current address: Earth and Environmental Sciences, Boston College, Chestnut Hill, MA 02467, USA

[4]Cooperative Institute for Marine Ecosystem and Resources Studies (CIMERS), Oregon State University, 2030 SE Marine Science Drive, Newport, Oregon 97365, USA

*Correspondence: clare.reimers@oregonstate.edu

Supplemental Method Details

Eddy covariance data processing

Velocities and other ADV outputs were recorded continuously at rates of 32 or 64 Hz during deployments. Simultaneously, the fiber-optic oxygen sensors were activated at pulsed LED flash rates of 10 Hz through PyroScience FireStingO_2-Subport modules enclosed in Delrin housings, and their analog outputs were sampled and recorded at the ADV sampling rate. Rockland Scientific (Victoria, BC, Canada) fabricated the fiber-optic sensor controlling units under their Microsquid product line.

The processing sequence used to derive benthic oxygen fluxes and to study the eddy covariance time-series data began by preparing calibration configuration files for each OXB430 sensor based on both "pre-" and "post-" deployment, in-laboratory, 0% and 100% air-saturation, sensor dPhi recordings (i.e., values that represent the phase shift of the sensor's NIR-emission relative to the red-light excitation) at a known temperature and atmospheric pressure. Next, these files were called by a Matlab function (provided by Rockland Scientific) to convert the sensor's deployment record into physical units. The function inputs were data vectors of the sensor's dPhi readings, temperature, salinity, and water depth, in addition to the configuration files.

Other scripts written in Matlab were used to divide data records into numbered 15- minute-long periods or "bursts"; replace by interpolation any outliers identified as spikes (Goring and Nikora 2002); and reduce the sampling to 8 Hz. Both pre- and post-calibration DO series in 8 Hz format were then compared to all available independent reference data. As described in Reimers and Fogaren (2021), a final oxygen series was resolved such that the accepted series was adjusted to be a weighted percent of the pre- and post-calibration series where the fractions of each were set to progressively shift to match reference measurements.

The concluding stage of processing was to compute the fluctuating components of the directional velocities [$v_x'(t), v_y'(t), v_z'(t)$] and oxygen concentrations [$C'(t)$] by subtracting long period trends [$\overline{v_x(t)}, \overline{v_y(t)}, \overline{v_z(t)}, \overline{C(t)}$] derived by 3 methods for each 15-minute burst. These methods represented the "means" of each 15-min series as either: (1) a linear trend, (2) a low-pass frequency filter (set to 0.002 Hz) (Reimers et al. 2012), or (3) a running mean (given a filter size set in this study to a 6.25 min moving time window). These different filters informed evaluations of how low-frequency oscillations may have contributed to or biased oxygen fluxes, with a focus on internal wave effects (expanded on below). The velocity series of each burst were also rotated by a 2-angle method (first around the *z*-axis, then around *y*-axis) that solves for rotation angles that minimize any surface wave frequency variations in $v_z'(t)$ (Reimers et al. 2012; Reimers and Fogaren 2021). Lastly, the oxygen data series of each burst was shifted in time relative to the rotated velocity data to a maximum of 2 seconds to achieve the greatest correlation (and thus maximum flux) per burst (Attard et al. 2014). These time shifts will ideally account for the separation of the OXB430 fiber-optic sensor relative to the velocity measurement volume and the inherent response lag of the OX430 sensor (Merikhi et al. 2018).

Final oxygen flux evaluations

Criteria to reject segments of eddy covariance data when deriving time series of benthic oxygen fluxes have been proposed in several studies (e.g., Attard et al. 2014; Huettel et al. 2020), with such criteria aimed to ultimately eliminate conditions that may invalidate the method's primary assumption, which is that eddy covariance fluxes reflect the sediment sink in an adjacent control volume dependent on the velocity field (Berg et al. 2007). Most often, bursts are examined individually and discounted or trimmed if they show evidence of oxygen sensor spikes or dips that may be caused by particle collisions, or abrupt changes in dissolved oxygen, flow speed and/or

direction, that while interesting, can contaminate fluxes (Holtappels et al. 2013; Attard et al. 2014; Huettel et al. 2020). This screening practice was applied in this study.

One complicating dynamic observed in all records from this study was low-frequency oscillations forced by internal waves. Pulses of internal wave velocity oscillations have been observed in prior measurements of this kind on the Oregon shelf (Reimers et al. 2016) and were discerned here to display wave periods averaging 12.5 min. In some cases, their effects resulted in outlier fluxes or caused fluxes to be sensitive to the three alternate detrending methods we routinely applied, which differed in how low frequencies were filtered. We used this sensitivity to help screen the time series, excluding bursts where the internal wave effects were acute, and this screening reduced the standard deviations of average fluxes. Overall, when reporting average fluxes in Table 2 of this study, from 0 to 9.2% of individual eddy covariance time series were excluded because of irregularities, and a 6.25 min running average (RA) filtering method was used as the final detrending approach to minimize internal wave frequency contributions likely to be unreflective of oxygen consumption by the seabed. The RA fluxes were equal to between 84 and 95% of comparable fluxes computed with linear detrending and 94-116% compared to trends from a 0.002 frequency filter.

Supplemental Tables

Table S1. Burst means of environmental and flow parameters across deployments.

Deployment	n	sv'_z (cm s^{-1})	sC' (µmol L^{-1})	DO (µmol L^{-1})	Hor. Speed (cm s^{-1})	RMS vel (cm s^{-1})	H_s (m)	u_* (cm s^{-1})	ε (m^2s^{-3})
1	96	0.31±0.12	0.036±0.015	46.7±2.3	5.0±2.4	2.1±0.9	0.29±0.03	0.28±0.15	6.6±8.7 E-07
2	92	0.33±0.12	0.053±0.017	48.6±2.9	4.9±2.7	2.1±0.7	0.29±0.03	0.36±0.17	8.4±11.1 E-07
3	110	0.31±0.11	0.049±0.020	46.3±0.8	3.3±1.7	2.5±0.9	0.70±0.11	0.36±0.13	8.2±11.1 E-07
4	108	0.29±0.10	0.063±0.030	24.7±1.2	4.6±2.5	2.5±0.7	0.40±0.07	0.28±0.12	3.7±4.1 E-07
5	72	0.51±0.14	0.135±0.069	75.3±6.9	4.9±1.7	3.4±1.1	0.49±0.05	0.46±0.20	2.6±2.0 E-06
6	90	0.64±0.19	0.079±0.032	41.0±6.0	8.3±2.3	3.8±0.7	0.70±0.07	0.45±0.18	7.8±7.7 E-06
7	122	0.43±0.11	0.045±0.011	17.0±2.9	5.0±2.2	2.9±0.6	0.57±0.08	0.31±0.15	2.1±2.0 E-06

Table S2. Pearson correlation coefficients and p-values between eddy covariance oxygen flux determinations of sediment oxygen consumption and parameters within deployments. Those in red are significant (p-value ≤0.05).

Deployment	sv'_z	sC'	Dir	DO	Hor. speed	RMS vel	H_s	u_*	ε
1	0.431 <0.0001	0.630 <0.0001	0.124 0.480	0.016 0.876	.262 0.010	0.324 0.001	-0.093 0.368	0.519 <0.0001	0.365 0.0003
2	0.371 0.0003	0.365 0.0003	0.105 0.600	-0.150 0.153	0.276 .0.008	0.371 .0003	-0.129 0.220	0.264 .011	0.166 0.115
3	-0.112 0.244	0.603 <0.0001	0.201 0.108	0.105 0.273	-0.128 0.181	0.0194 0.841	-0.155 0.105	-0.0065 0.947	-0.164 0.086
4	0.238 0.013	0.193 0.045	0.443 <0.0001	-0.151 0.118	0.080 0.410	0.353 0.0002	0.260 0.0065	0.275 0.0040	0.337 .0004
5	0.510 <0.0001	0.365 0.0016	0.324 0.023	0.079 0.510	0.422 0.0002	0.217 0.067	0.061 0.613	0.575 <0.0001	0.375 0.0012
6	0.368 0.0004	0.546 <0.0001	0.278 0.031	0.264 0.012	0.284 0.0067	0.403 <0.0001	-0.090 0.399	0.569 <0.0001	0.281 0.0074
7	0.357 <0.0001	0.269 0.0027	0.168 0.180	0.166 0.067	0.409 <0.0001	0.384 <0.0001	0.077 0.399	0.517 <0.0001	0.189 0.037

Table S3. Correlation coefficients and p-values between deployment mean eddy covariance oxygen flux determinations expressed as positive Sediment Oxygen Consumption rates (i.e., +3.5 to +23.0 mmol $m^{-2}d^{-1}$) and means of environmental parameters. *significant correlation (p value <0.05)

Environmental parameter	**Pearson Correlation Coefficient (*r*)**	**p-value**	**Number of observations (n)**
DO (µmol L^{-1})	0.68	0.10	7
ADV Pressure (dbar)	-0.78	0.04*	7
H_s (m)	0.26	0.57	7
ε (m^2 s^{-3})	0.51	0.24	7
sv_z' (cm s^{-1})	0.73	0.06	7
sC' (µmol L^{-1})	0.97	0.0003*	7
Hor. Speed (cm s^{-1})	0.37	0.42	7
u_* (cm s^{-1})	0.83	0.02*	7
RMS Velocity (cm s^{-1})	0.77	0.04*	7

Table S4. Correlation coefficients and p-values between median grain size, mean macrofaunal abundance and richness, and several environmental characteristics of the four sites sampled in 2022. Those in red are significant (p-value ≤0.05).

		Median Grain Size	Abundance	Richness
SOC	**Pearson Corr.** **p-value**	0.48 0.52	0.51 0.49	0.45 0.55
DO	**Pearson Corr.** **p-value**	0.58 0.42	0.39 0.61	0.31 0.69
Pressure	**Pearson Corr.** **p-value**	0.31 0.69	-0.31 0.69	-0.50 0.50
H_s	**Pearson Corr.** **p-value**	-0.45 0.55	0.87 0.13	0.95 0.05
Turb. Diss. ε	**Pearson Corr.** **p-value**	-0.06 0.94	0.98 0.02	0.95 0.05
RMS Velocity	**Pearson Corr.** **p-value**	0.02 0.98	0.97 0.03	0.96 0.04
sv_z'	**Pearson Corr.** **p-value**	-0.09 0.91	0.97 0.03	0.99 0.01
sC'	**Pearson Corr.** **p-value**	0.64 0.36	0.32 0.68	0.23 0.77
Hor. Speed	**Pearson Corr.** **p-value**	-0.04 0.96	0.93 0.07	0.87 0.13
u_*	**Pearson Corr.** **p-value**	0.30 0.70	0.83 0.17	0.78 0.22
Median Grain Size	**Pearson Corr.** **p-value**		0.05 0.95	-0.23 0.77
Abundance	**Pearson Corr.** **p-value**	0.05 0.95		0.95 0.046
Richness	**Pearson Corr.** **p-value**	-0.23 0.77	0.95 0.046	

Supplemental Figures

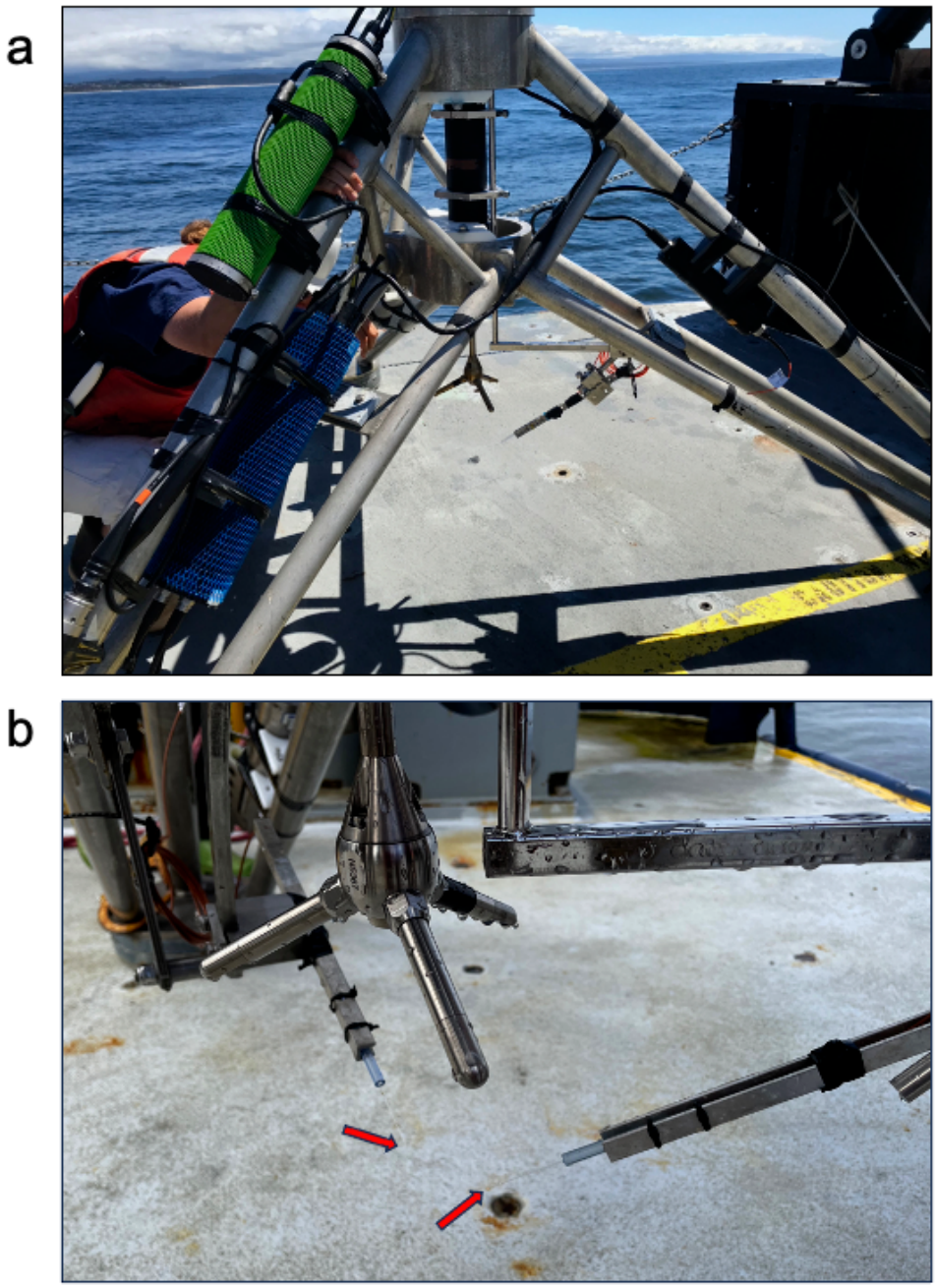

Fig. S1. Images of eddy covariance sensors with (a) single and (b) two fiber optic oxygen sensors positioned around the *Vector* sampling volume. Red arrows in (b) point to sensor tips.

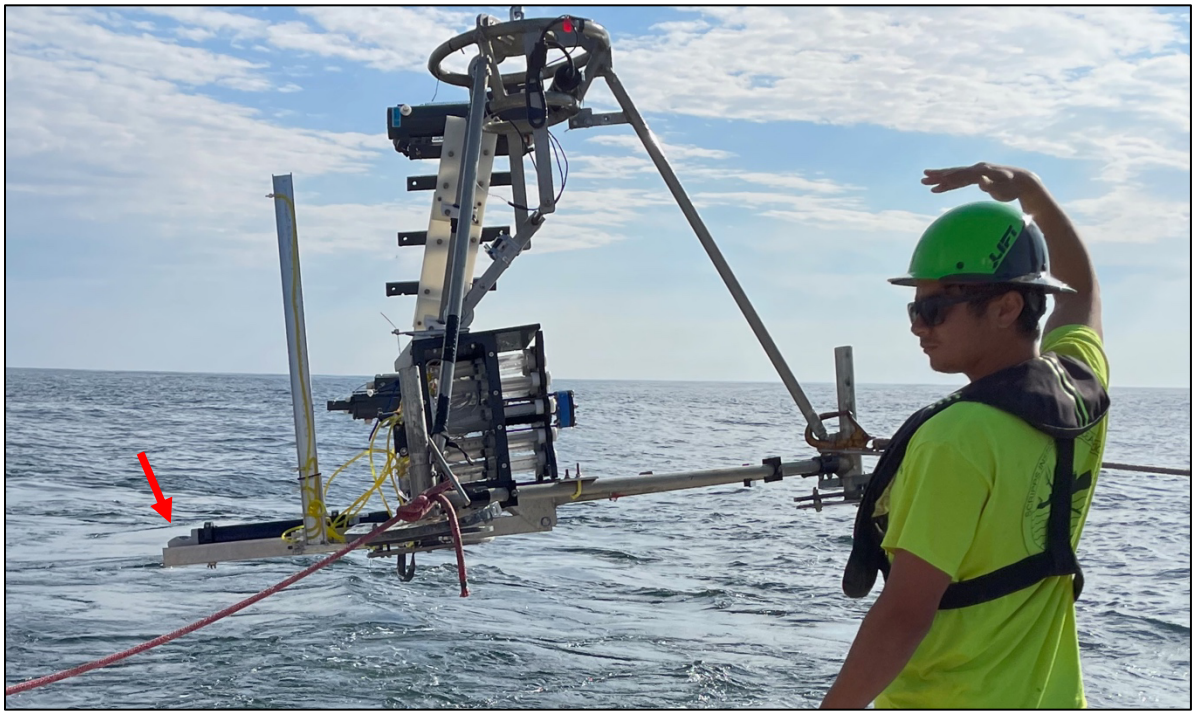

Fig. S2. Image of the Aquadopp Profiler 1 MHz, extended to the left, off a deployment tripod. A red arrow points to the sensor head. A device for collecting water samples at varying heights with inlets along a 1-m vertical mast was also mounted on the tripod after the design of Knoery et al. (2019).

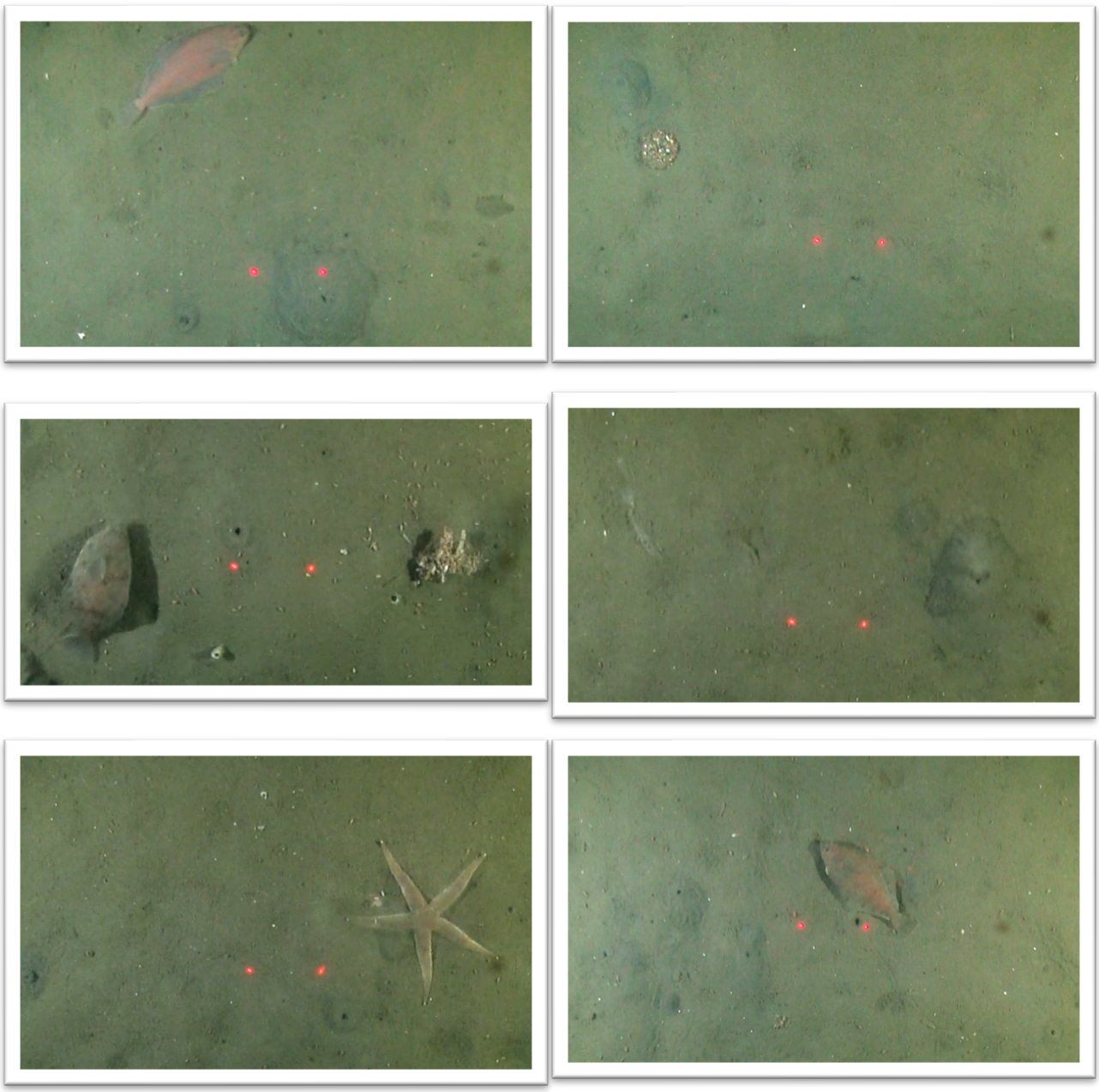

Fig. S3. Video screen-grab images of the seafloor on the NH line at 80 m showing flatfishes (clockwise from upper left: Rex sole *Glyptocephalus zachirus* and two Pacific sanddabs *Citharichthys sordidus*), an anemone, mounds, borrows, tubes, a sea star (*Luidia foliolata)*, coiled gastropods, and a decaying pyrosome. Laser spot separation is 10 cm.

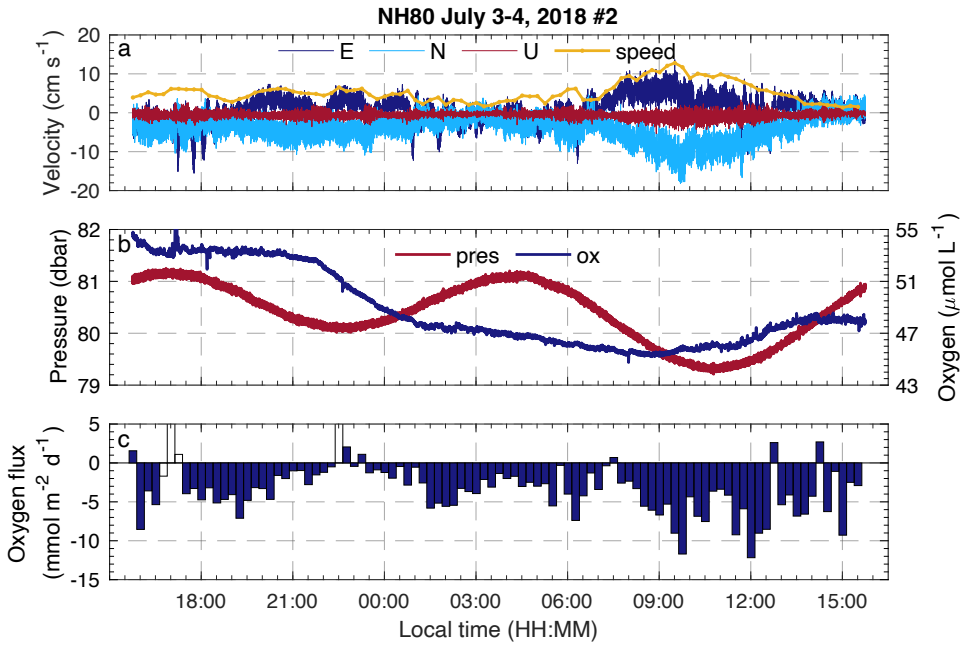

Fig. S4. Time series of eddy covariance sensor measurements at NH80 in July 2018 (deployment #2). Panel a) velocities in East-North-Up Cartesian coordinates and mean horizontal speed for each 15-min segment, b) pressure and dissolved oxygen at 8 Hz, c) derived oxygen fluxes for 15-min segments. White bars indicate calculated fluxes of segments omitted from deployment flux averages.

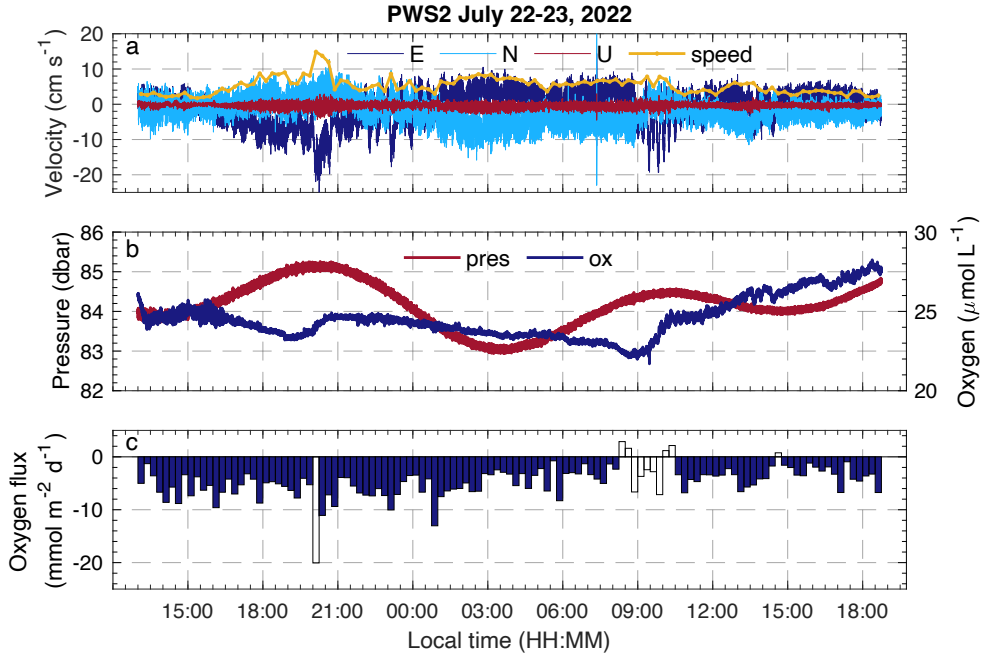

Fig. S5. Time series of eddy covariance sensor measurements at PWS2 in July 2022 (deployment #4). Panels are as in Fig. S4.

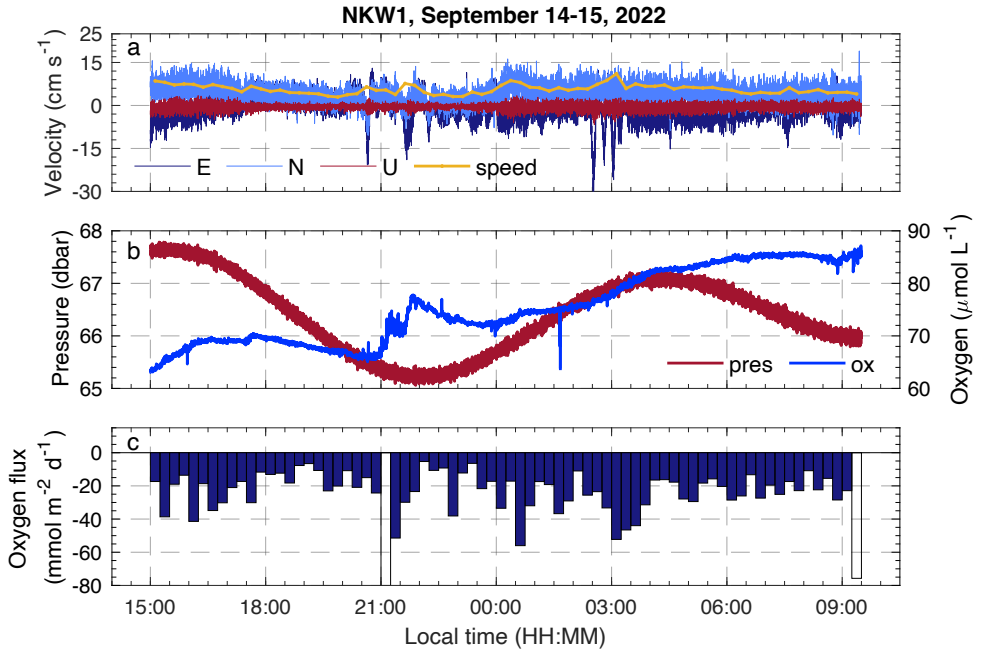

Fig. S6. Time series of eddy covariance sensor measurements at NKW1 in September 2022 (deployment #5). Panels are as in Fig. S4.

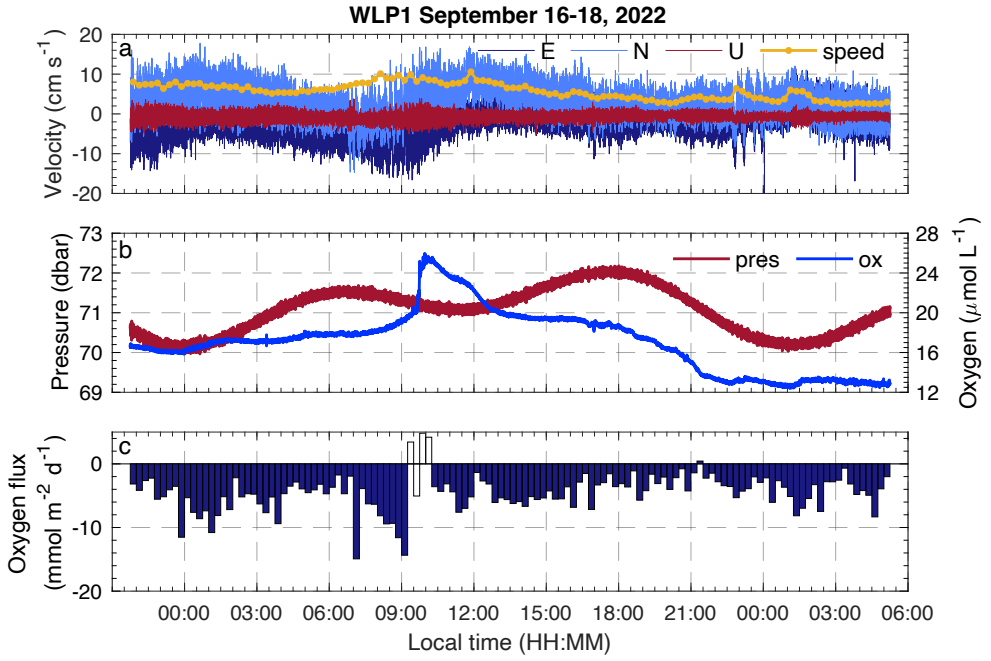

Fig. S7. Time series of eddy covariance sensor measurements at WLP1 in September 2022 (deployment #7). Panels are as in Fig. S4.

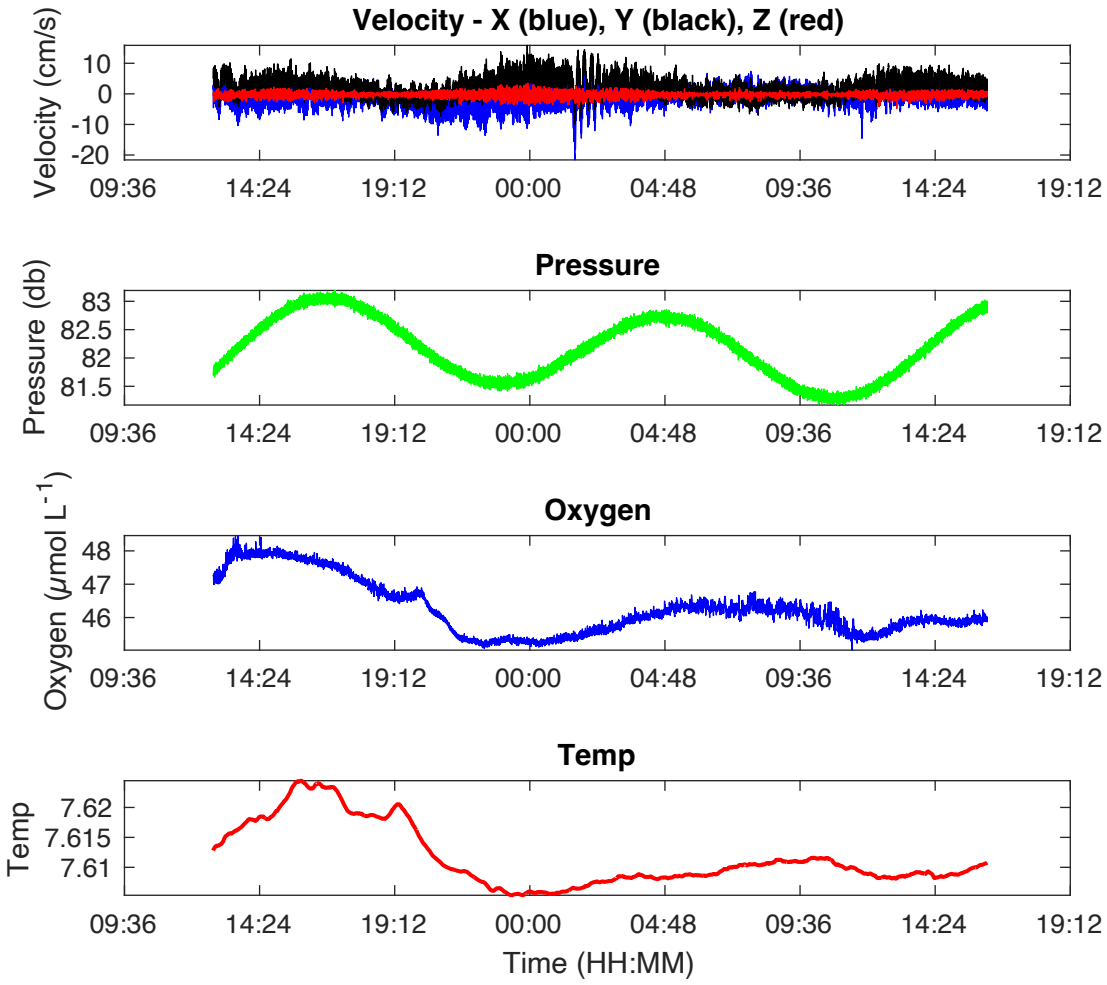

Fig. S8. Deployment 3 primary time series including temperature in °C.

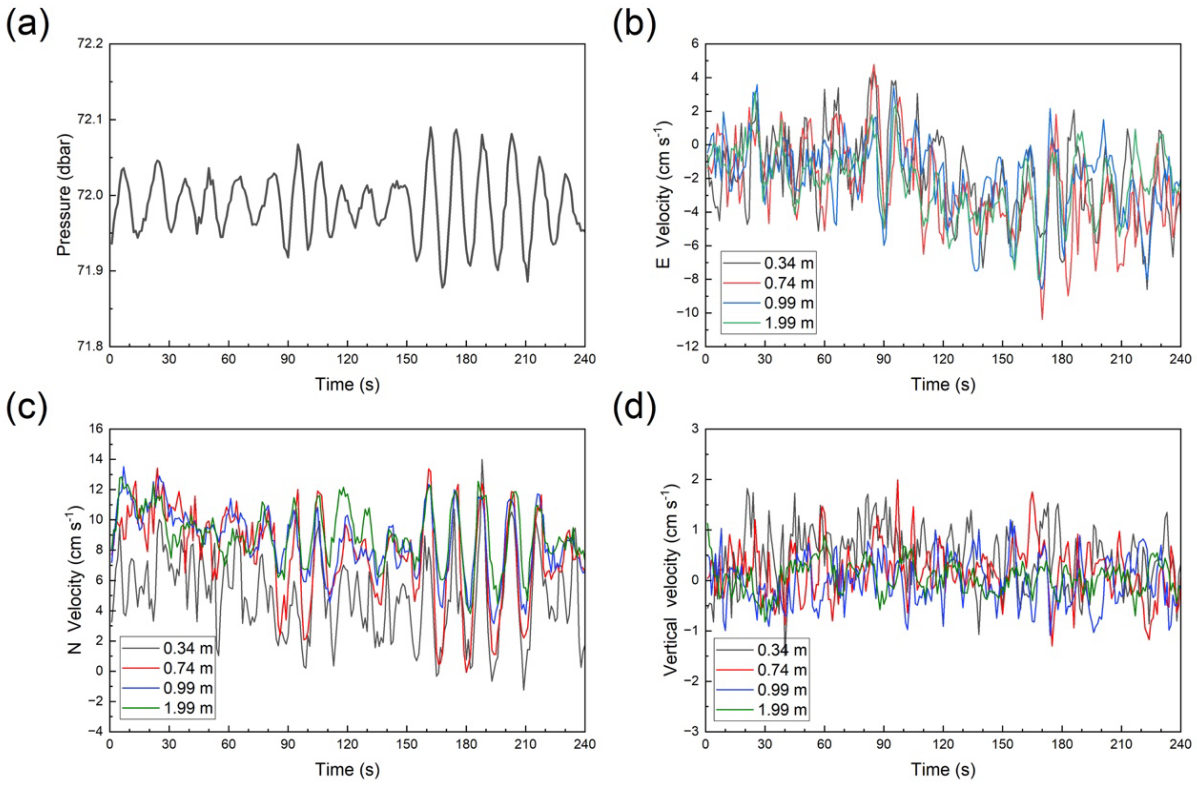

Fig. S9. Example of Aquadopp Profiler time-series data. Displayed are (a) Pressure, and (b) E velocity, (c) N velocity and (d) Vertical velocity (+Up) at four heights at WLP 1.

References within Supporting Information

Attard, K. M., R. N. Glud, D. F. McGinnis, and S. Rysgaard. 2014. Seasonal rates of benthic primary production in a Greenland fjord measured by aquatic eddy correlation. *Limnology and Oceanography* **59**: 1555-1569. https://doi.org/10.4319/lo.2014.59.5.1555

Berg, P., H. Røy, and P. L. Wiberg. 2007. Eddy correlation flux measurements: The sediment surface area that contributes to the flux. *Limnology and Oceanography* **52**: 1672-1684. https://doi.org/10.4319/lo.2007.52.4.1672

Goring, D. G., and V. I. Nikora. 2002. Despiking acoustic Doppler velocimeter data. *Journal of Hydraulic Engineering* **128**: 117–126. https://doi.org/10.1061/(ASCE)0733-9429(2002)128:1(117)

Huettel, M., P. Berg, and A. Merikhi. 2020. Technical note: Measurements and data analysis of sediment-water oxygen flux using a new dual-optode eddy covariance instrument. *Biogeosciences* **17**: 4459-4476. https://doi.org/10.5194/bg-17-4459-2020

Knoery, J., D. Cossa, B. Thomas, G. Gregory, and S. Rigaud. 2019. SUSANE, a device for sampling chemical gradients in the benthic water column. *Limnology and Oceanography: Methods* **17:** 331-342. https://doi.org/10.1002/lom3.10317

Merikhi, A., P. Berg, V. Meyer, and M. Huettel. 2018. Jet-nozzle method for measuring response times of scalar sensors used in liquids and gases. *Limnology and Oceanography: Methods* **16**: 475–483. https://doi.org/10.1002/lom3.10259

Reimers, C..E. and K. E. Fogaren. 2021. Bottom boundary layer oxygen fluxes during winter on the Oregon shelf. *Journal of Geophysical Research-Oceans* **126**: e2020JC016828. https://doi.org/10.1029/2020JC016828

Reimers, C. E., H. T. Özkan-Haller, P. Berg, A. Devol, K. McCann-Grosvenor, and R. D. Sanders. 2012. Benthic oxygen consumption rates during hypoxic conditions on the Oregon continental shelf: Evaluation of the eddy correlation method. *Journal of Geophysical Research- Oceans* **117**: C02021, https//doi.org/10.1029/2011JC007564

Reimers, C. E., H. T. Özkan-Haller, R. D. Sanders, K. McCann-Grosvenor, K., P. J. Chace, and S. A. Crowe. 2016. The dynamics of benthic respiration at a mid-shelf station off Oregon. *Aquatic Geochemistry* **22**: 505-527. https://doi.org/10.1007/s10498-016-9303-5